

# Revealing the sub-AU asymmetries of the inner dust rim in the disk around the Herbig Ae star R Coronae Austrinae<sup>★</sup>

S. Kraus<sup>1</sup>, K.-H. Hofmann<sup>1</sup>, F. Malbet<sup>2</sup>, A. Meilland<sup>3,1</sup>, A. Natta<sup>4</sup>, D. Schertl<sup>1</sup>, P. Stee<sup>3</sup>, and G. Weigelt<sup>1</sup>

<sup>1</sup> Max Planck Institut für Radioastronomie, Auf dem Hügel 69, 53121 Bonn, Germany  
e-mail: skraus@mpi.fr-bonn.mpg.de

<sup>2</sup> Laboratoire d'Astrophysique de Grenoble, UMR 5571 Université Joseph Fourier/CNRS, BP 53, 38041 Grenoble Cedex 9, France

<sup>3</sup> UMR 6525 H. Fizeau, Univ. Nice Sophia Antipolis, CNRS, Observatoire de la Côte d'Azur, Av. Copernic, 06130 Grasse, France

<sup>4</sup> INAF – Osservatorio Astrofisico di Arcetri, Largo Fermi 5, 50125 Firenze, Italy

Received 26 July 2009 / Accepted 28 October 2009

## ABSTRACT

**Context.** Unveiling the structure of the disks around intermediate-mass pre-main-sequence stars (Herbig Ae/Be stars) is essential for our understanding of the star and planet formation process. In particular, models predict that in the innermost AU around the star, the dust disk forms a “puffed-up” inner rim, which should result in a strongly asymmetric brightness distribution for disks seen under intermediate inclination.

**Aims.** Our aim is to constrain the sub-AU geometry of the inner disk around the Herbig Ae star R CrA and search for the predicted asymmetries.

**Methods.** Using the VLTI/AMBER long-baseline interferometer, we obtained 24 near-infrared (*H*- and *K*-band) spectro-interferometric observations on R CrA. Observing with three telescopes in a linear array configuration, each data set samples three equally spaced points in the visibility function, providing direct information about the radial intensity profile. In addition, the observations cover a wide position angle range ( $\sim 97^\circ$ ), also probing the position angle dependence of the source brightness distribution.

**Results.** In the derived visibility function, we detect the signatures of an extended (Gaussian *FWHM*  $\sim 25$  mas) and a compact component (Gaussian *FWHM*  $\sim 5.8$  mas), with the compact component contributing about two-thirds of the total flux (both in *H*- and *K*-band). The brightness distribution is highly asymmetric, as indicated by the strong closure phases (up to  $\sim 40^\circ$ ) and the detected position angle dependence of the visibilities and closure phases. To interpret these asymmetries, we employ various geometric as well as physical models, including a binary model, a skewed ring model, and a puffed-up inner rim model with a vertical or curved rim shape. For the binary and vertical rim model, no acceptable fits could be obtained. On the other hand, the skewed ring model and the curved puffed-up inner rim model allow us to simultaneously reproduce the measured visibilities and closure phases. From these models we derive the location of the dust sublimation radius ( $\sim 0.4$  AU), the disk inclination angle ( $\sim 35^\circ$ ), and a north-south disk orientation (PA  $\sim 180$ – $190^\circ$ ). Our curved puffed-up rim model can reproduce reasonably well the interferometric observables and the SED and suggests a luminosity of  $\sim 29 L_\odot$  and the presence of relatively large ( $\geq 1.2 \mu\text{m}$ ) Silicate dust grains. Our study also reveals discrepancies between the measured interferometric observables and the puffed-up inner rim models, providing important constraints for future refinements of these theoretical models. Perpendicular to the disk, two bow shock-like structures appear in the associated reflection nebula NGC 6729, suggesting that the detected sub-AU size disk is the driving engine of a large-scale outflow.

**Conclusions.** Detecting, for the first time, strong non-localized asymmetries in the inner regions of a Herbig Ae disk, our study supports the existence of a puffed-up inner rim in YSO disks.

**Key words.** stars: pre-main-sequence – circumstellar matter – accretion, accretion disks – planetary systems: protoplanetary disks – planetary systems: formation – techniques: interferometric

## 1. Introduction

For our understanding of the structure and physical processes in the disks around young stellar objects (YSOs), the inner-most disk regions are of special importance. Furthermore, it is believed that planet formation is a direct result of the grain aggregation and growth which should take place in the inner few AUs of the dusty disks around these stars. As the spatial scales of the inner circumstellar environment were not accessible to imaging observations until recently, most conclusions drawn on the geometry of the inner disk were based on the modeling of

the spectral energy distribution (SED). Typically, the SED of intermediate-mass YSOs (Herbig Ae/Be stars) shows a characteristic infrared excess emission, which is often interpreted as the presence of a circumstellar accretion disk, although the 3D geometry of the innermost (AU-scale) region of these disks is still poorly known.

According to the current paradigm, most of the infrared excess emission in Herbig Ae/Be stars originates from a passive dust disk (Adams et al. 1987), whose thermal structure can be approximated with a cold disk interior and a hot surface layer (Chiang & Goldreich 1997). To fulfill vertical hydrostatic equilibrium, the disk is expected to flare towards larger radii, allowing the outer disk regions to intercept more stellar light than expected for a geometrically flat disk (Kenyon & Hartmann 1987). At a certain distance from the star, most often

<sup>★</sup> Based on observations made with ESO telescopes at the La Silla Paranal Observatory under programme IDs 079.D-0370(A), 081.C-0272(A,B,C), and 081.C-0321(A).

referred to as the dust sublimation radius  $R_{\text{subl}}$ , the dust temperature will exceed the evaporation temperature of dust ( $T_{\text{subl}}$ ), causing the truncation of the dust disk and the formation of a dust-free inner hole. This scenario also gained support from the first survey-type near-infrared interferometric observations of Herbig Ae/Be stars. Millan-Gabet et al. (2001) could measure the characteristic size of many YSO disks, finding that the measured sizes scale roughly with the square-root of the luminosity  $L_*$  of the stellar source (Monnier & Millan-Gabet 2002). Since this is the expected scaling-relation for the location of the dust-sublimation radius ( $R_{\text{subl}} \propto L_*^{1/2}$ ), this finding supports the idea that the near-infrared emission is tracing mainly hot material located in a structure at the location of the dust sublimation radius. More recently, significant deviations from the size-luminosity were detected concerning, in particular, the T Tauri and Herbig Be star regime (Monnier et al. 2005). These deviations might be explained either with contributions from scattered light (most important for T Tauri stars; e.g. Pinte et al. 2008) or from a gaseous disk located inside of the dust sublimation radius (more important for Herbig Be stars; see e.g. Akesson et al. 2005; Eisner et al. 2007; Kraus et al. 2008; Isella et al. 2008; Tannirkulam et al. 2008).

In 2001, Natta et al. and Dullemond et al. pointed out that the heating provided by the stellar radiation should considerably increase the disk scale height close to the dust sublimation radius, resulting in the formation of a “puffed-up” inner rim. This rim might cast a shadow on the more extended disk regions, possibly affecting the thermal disk structure out to hundreds of AUs. The shadowing effects of the puffed-up rim might already have been observed indirectly in the SED. Meeus et al. (2001) argued that the general shape of the SED of many Herbig Ae/Be stars can be divided into two groups, where “group I” sources show a pronounced  $60 \mu\text{m}$  bump, while “group II” sources have a flatter SED, lacking the  $60 \mu\text{m}$  excess emission. Later, Dullemond & Dominik (2004) pointed out that this empirical classification could be explained by considering both the flaring properties of the outer disk and the shadowing effects of a puffed-up inner rim. Accordingly, group I disks might exhibit a strongly flared shape, allowing the outer disk to step out of the shadow region, while group II disks are fully self-shadowed.

Although these studies provided some important first insight, there are major uncertainties concerning both the magnitude of the puffing-up effect as well as the detailed rim shape. For instance, it was proposed that density-dependent dust sublimation effects (Isella & Natta 2005, referred to as IN05 in the following) as well as grain growth and dust sedimentation (Tannirkulam et al. 2007) could affect the shape of the inner rim, resulting in a curved vertical rim geometry. In a recent study, Kama et al. (2009) found that backwarming effects and the presence of highly refractory grain species might result in a dust rim which is located significantly closer to the star than anticipated in earlier studies. Using radiative transfer, they show that the rim is not an infinitely sharp wall, but has an optically thin region which might extend a significant fraction of the rim radius, resulting in a more diffuse rim morphology. Spatially resolved observations are required to directly measure the shape of the inner rim. Furthermore, various authors (e.g. Miroshnichenko et al. 1999) have pointed out that the infrared emission of many Herbig Ae/Be stars might contain significant scattered-light contributions from optically thin circumstellar envelopes or halos. As investigated by Vinković et al. (2003) and others, high-angular resolution imaging observations, such as presented in this study, provide the only method to separate the disk and

envelope contributions and to solve the ambiguities inherent to pure SED model fits.

One of the strongest predictions which is common to all puffed-up rim scenarios is the appearance of asymmetries in the source brightness distribution for disks seen under an intermediate inclination angle. This “skew” in the brightness distribution is a direct consequence of the vertical extension of the rim above the disk midplane, providing perhaps the most promising way to observationally distinguish between scenarios with and without a puffed-up rim. In order to detect these signatures, infrared interferometry provides not only the required milli-arcsecond (mas) angular resolution, but also offers a very sensitive measure for deviations from point-symmetry, namely the closure phase (CP) relation (Jennison 1958). First closure phase measurements on YSOs were presented by Monnier et al. (2006). Using the IOTA interferometer and baseline lengths up to 38 m, these authors measured statistically significant non-zero closure phases on six out of 14 stars (excluding binary stars). For five of these six stars, the detected closure phase signals were rather small ( $\Phi \lesssim 5^\circ$ ), while for the Be star HD 45677 phases of up to  $\sim 27^\circ$  could be detected.

In order to investigate the geometry of the inner circumstellar environment around a Herbig Ae star in great detail and to obtain further evidence for or against the existence of a puffed-up inner rim, we have studied the Herbig Ae star R CrA using ESO’s Very Large Telescope Interferometer (VLTI) and the AMBER beam combination instrument. In the following, we will first summarize some earlier studies on R CrA (Sect. 2), followed by a description of our interferometric observations (Sect. 3) and the employed models (Sect. 4). Finally, we will discuss our modeling results (Sect. 5) and conclude with a brief summary (Sect. 6).

## 2. Earlier studies on R CrA

R CrA is located in the Corona Australis molecular cloud and is the most luminous ( $L_{\text{bol}} \sim 99 L_\odot$ , Bibo et al. 1992) star of the very young and obscured cluster known as the Coronet cluster (Taylor & Storey 1984). The stellar parameters of R CrA are still rather uncertain, ranging from a spectral type of F5 (Hillenbrand et al. 1992; Natta et al. 1993; Garcia Lopez et al. 2006), A5 (Herbig & Bell 1988; Chen et al. 1997) to B8 (Bibo et al. 1992; Hamaguchi et al. 2005). For the distance, we adopt the commonly assumed value of 130 pc (Marraco & Rydgren 1981).

Compared to other stars in the Herbig Ae/Be class, R CrA is in a particularly early evolutionary phase (Malfait et al. 1998) and still embedded in an extended and massive natal envelope, whose emission dominates the SED from mid-infrared to millimeter-wavelengths (Fig. 12, bottom, left). Natta et al. (1993) estimated the mass of the envelope to be  $\sim 10 M_\odot$  with an outer envelope radius of 0.007 pc ( $\sim 1450$  AU). In the classification scheme of Meeus et al. (2001), R CrA was classified as a group II object (Acke & van den Ancker 2004), suggesting the presence of a disk with a pronounced inner rim, which might self-shadow the outer disk. Optical polarization measurements showed a high degree of linear ( $\sim 8\%$ ) and circular ( $\sim 5\%$ ) polarization (Ward-Thompson et al. 1985; Clark et al. 2000), indicating scattering from aligned, non-spherical dust grains. The polarization mapping also showed an extended ( $\sim 10''$ ), disk-like structure with north-south orientation ( $\theta = 189 \pm 5^\circ$ , Ward-Thompson et al. 1985). The total mass of gas and dust in the disk was estimated from sub-millimeter observations by Mannings (1994), yielding  $0.02 M_\odot$ . More recently, Groppi et al. (2007) used the SMA to derive an upper mass limit of  $0.012 M_\odot$ .

At optical wavelengths, the star is known to be highly variable both on long and short time scales (Bellingham & Rossano 1980). Graham & Phillips (1987) reported strong variability in the  $H\alpha$  line of R CrA as well as surface brightness variations in the nearby reflection nebula NGC 6729, possibly indicating shadowing effects caused by material in the inner circumstellar environment of R CrA or clumpy accretion (Graham 1992). Variability was also observed at radio- and X-ray wavelengths (Forbrich et al. 2006). The X-ray spectrum of R CrA is very unusual, including a very hot X-ray emission component. Intermediate-mass YSOs are expected to show no X-ray emission, since they should possess neither magnetically driven coronae nor the radiation-driven winds which cause X-ray-emitting shock regions. Therefore, in order to explain the detected X-ray spectrum, Forbrich et al. (2006) suggested that the X-ray emission does not originate from the optical/infrared source, but from a yet undiscovered Class I companion. The presence of a close companion was also proposed by Takami et al. (2003) based on spectro-astrometric observations which revealed a photo-center displacement<sup>1</sup> both in the blue- and red-shifted wing of the spectrally resolved  $H\alpha$ -line. The authors pointed out that the detected signature cannot be explained with a stellar companion or an outflow component alone, but possibly with a combination of both scenarios. However, as pointed out by Choi et al. (2008), it is unlikely that the companion proposed by Takami et al. (2003) is identical to the Class I companion proposed by Forbrich et al. (2006), since a deeply embedded Class I source would not contribute significantly to the  $H\alpha$  line flux at visual wavelengths.

The accretion activity of R CrA was estimated by Garcia Lopez et al. (2006) from the luminosity of the Br $\gamma$ -line, yielding a relatively low accretion luminosity of  $L_{\text{acc}} = 3.2 L_{\odot}$ , corresponding to a mass accretion rate of  $\dot{M}_{\text{acc}} = 10^{-7.12} M_{\odot}/\text{yr}$  (for a F5 star). Besides indications of active accretion, various outflow tracers have been reported for R CrA. For instance, a compact bipolar molecular outflow with an east-west orientation (Walker et al. 1984; Levreault 1988; Graham 1993) as well as several Herbig-Haro objects (in particular HH 104 A/B) have been associated with R CrA (Hartigan & Graham 1987; Graham 1993). However, more recent studies (Anderson et al. 1997; Wang et al. 2004), convincingly identified the source IRS 7 as driving source of these outflows, making a physical association with R CrA rather unlikely.

### 3. Observations

We observed R CrA during four nights in June 2008 using the VLTI near-infrared interferometric instrument AMBER (Petrov et al. 2007), which combines the light from three of the 1.8 m auxiliary telescopes (ATs). For all observations, AMBER's low spectral resolution mode (LR-HK) with a spectral resolution of  $\lambda/\Delta\lambda = 35$  and a wavelength coverage from 1.4 to 2.5  $\mu\text{m}$  ( $H$ - and  $K$ -band) was used. The telescopes were placed on stations E0-G0-H0, forming a linear array configuration with baseline lengths of 16 (E0-G0), 32 (H0-G0), and 48 m (E0-H0). Due to this linear telescope arrangement and the spectral coverage provided by the AMBER instrument, each of our AMBER observations provides a good sampling of the  $uv$ -plane towards a certain position angle (PA), covering spatial frequencies between  $\sim 4$  and  $25 \times 10^6 \lambda$ , allowing one to cover a wide range of the visibility function ( $0.8 \lesssim V \lesssim 0.1$ ). By obtaining a large number of observations towards different hour angles, we also achieved

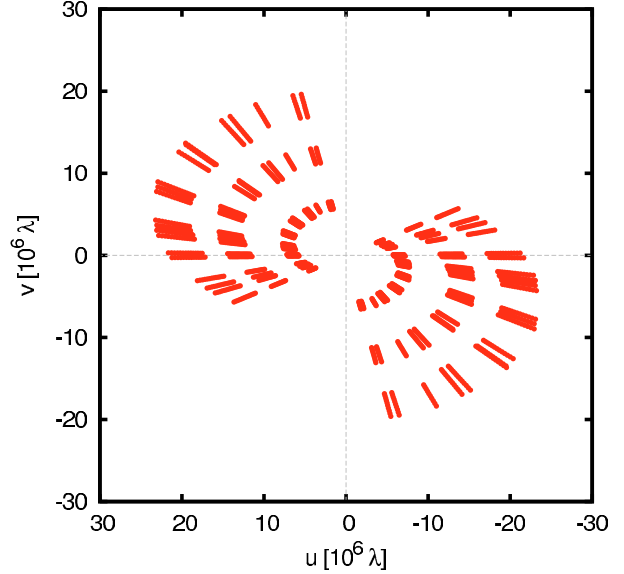


**Fig. 1.**  $uv$ -plane coverage obtained with our VLTI/AMBER observations on R CrA ( $K$ -band only).

a good PA coverage, probing PAs between  $16^\circ$  and  $113^\circ$  (Fig. 1). In order to adjust for changing atmospheric conditions and to test for possible systematic effects, we recorded data with different detector integration times (DITs), namely 50 ms (default value), 100 ms, and 200 ms.

The science observations on R CrA were interlaid with observations on interferometric calibrator stars, allowing us to monitor the instrumental transfer function. The transfer function is used in the course of data reduction to correct for wavelength-dependent instrumental or atmospheric effects. Each observation block (either on R CrA or on the calibrator star) typically consisted of five data sets, each containing 1000 (for DIT = 50 ms) or 500 (for DIT = 100 ms or DIT = 200 ms) individual spectrally dispersed interferograms.

For data reduction, we used the *amdlib* data reduction software (release 2.2). This software employs the P2VM algorithm (Tatulli et al. 2007) to derive wavelength-dependent visibilities and closure phases (CP). The wavelength calibration was done using the procedure described in Appendix A of Kraus et al. (2009). Following the standard AMBER data reduction procedure, we select the 10% of interferograms with the best signal-to-noise (SNR) ratio. Furthermore, we reject interferograms which were taken with an optical path delay (OPD) larger than 4  $\mu\text{m}$  in order to avoid systematic degenerative effects. To determine the transfer function, we first plot the observables for a representative spectral channel as a function of time (Fig. 2). Then, we reject observation blocks which show a significant intrinsic scatter between the five individual exposures, typically indicating some degraded quality due to poor atmospheric conditions. While very few observations have to be rejected for the  $K$ -band, only a few  $H$ -band measurements provide reliable results, reflecting the lower brightness of the object in this spectral window and the lower stability of the atmosphere at shorter wavelengths. Finally, we correct for the intrinsic diameters of the calibrator stars used (Table 1) and average the diameter-corrected calibrator observations for each night and for each spectral channel in order to yield the transfer function. The calibration error is estimated from the scatter of the individual calibrator observations over the night. As can be seen in Fig. 2, the calibration uncertainty is typically about  $\sim 3\%$  for

<sup>1</sup> Earlier spectro-astrometric observations were presented by Bailey (1998), but did not show this spectro-astrometric signature.

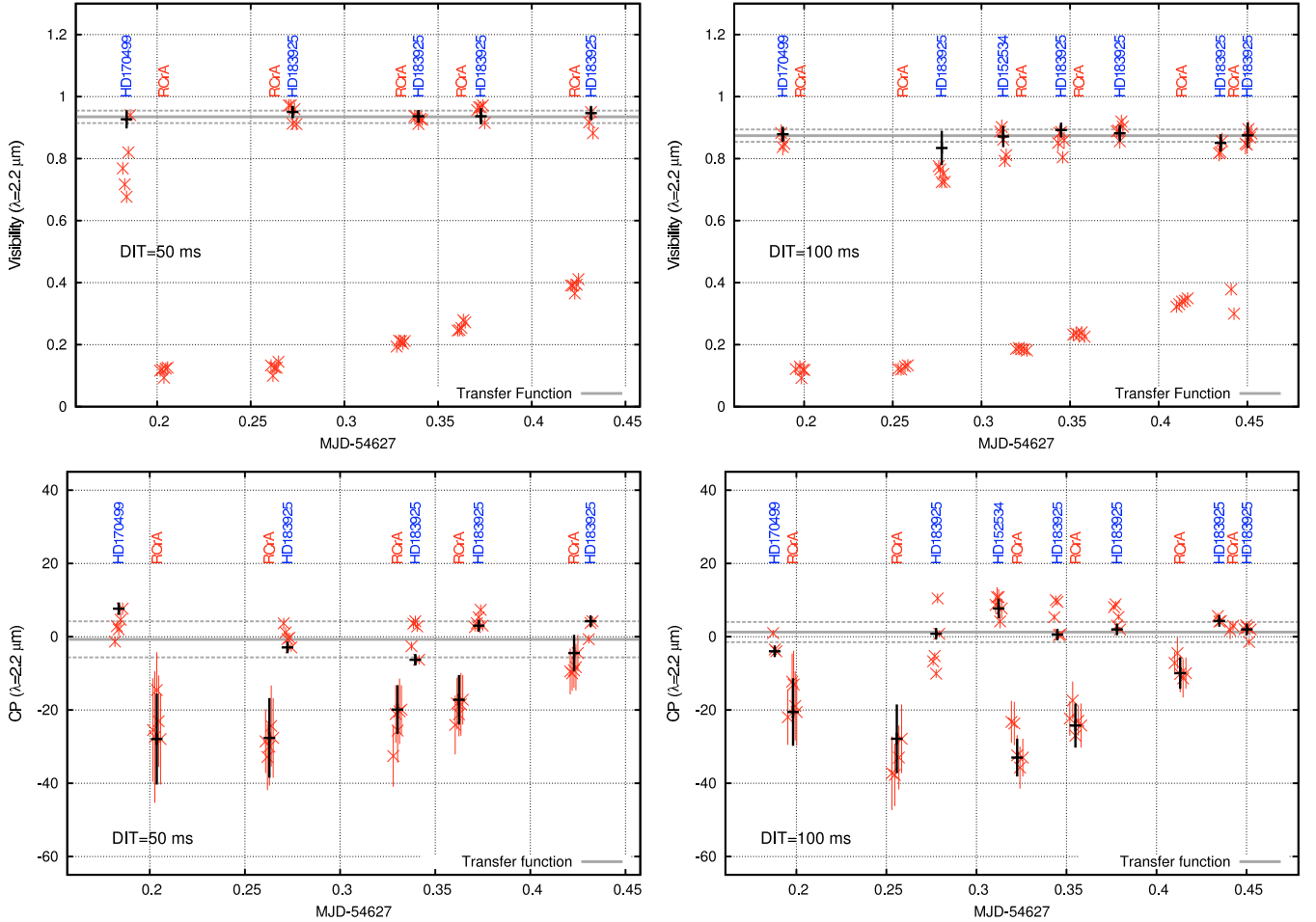


**Fig. 2.** Transfer function of the night 2008-06-09 for one spectral channel around  $2.2 \mu\text{m}$  and observations with DITs of 50 ms (left) and 100 ms (right). The visibilities measured on the longest baseline (top) and closure phases (bottom) are plotted as a function of time over the night. For each block of five exposures (red data points), we compute the average observables and correct the calibrator visibilities to correct for their intrinsic UD diameters (black crosses). After rejecting data sets with strong intrinsic scatter, we average the calibrator measurements to compute the instrumental transfer function (grey line).

visibility and  $\sim 5^\circ$  for CPs. Besides this calibration error, we include the statistical error estimate provided by *amdlb*. Since this procedure results in unrealistically small error bars for some individual measurements, we add a constant calibration uncertainty of 3% for the visibility measurements. As can be seen in Fig. 2, the measurements obtained with different DIT values agree very well with each other, indicating good data quality.

For some of our observations on R CrA, we employed the AMBER beam commutation device (BCD, Petrov et al. 2007). This calibration device allows one to exchange the beams of two of the three telescopes within a few seconds and to trace potential drifts in the CP transfer function on much shorter time scales than a typical VLTI target/object cycle ( $\sim 30$  min). Furthermore, the BCD device is located close to the beginning of the optical path of the AMBER instrument and inverts the phase sign of the two exchanged beams, while the instrument-internal phases are not affected (Millour et al. 2008). Due to this optically introduced change in the CP sign, it is possible to distinguish real astrophysical CP signatures from potential systematic instrumental artifacts. Our BCD observations on R CrA were performed on 2008-06-02 and show the expected change of sign (Fig. 3), confirming the astrophysical origin of the detected CP signals.

Figure 4 shows the position angle dependence of the derived visibilities and CPs for two spectral windows around 2.0 and

$2.2 \mu\text{m}$ . In order to interpret these position angle dependent variations, it is necessary to model the object morphology, taking also the variations of the projected baseline length with position angle into account, as will be done in Sect. 4. In Fig. 5 (left), we plot the visibilities measured for the PA range  $83^\circ$ – $113^\circ$  as a function of spatial frequency. The spatial frequency  $\nu = B/\lambda$  provides a measure for the resolving power achieved with a certain observation and is therefore proportional to the projected baseline length and inverse proportional to the observing wavelength  $\lambda$ . As can be seen in the left panel, the visibilities measured for different spectral channels in the *H*- and *K*-band can be very well represented with the same visibility profile. This indicates that the brightness distribution does not show a strong wavelength dependence<sup>2</sup>, which has interesting implications on the temperature-distribution of the emitting physical structure (see discussion in Sect. 5.3). Given the relatively small number of reliable *H*-band measurements, we consider only the *K*-band measurements for the following quantitative modeling. Also, the measured *H*-band closure phases are associated with very large error bars and are therefore omitted for the quantitative analysis.

<sup>2</sup> This argument is valid only for the visibility function  $V$ , but might not apply to the wavelength dependence of the closure phases, which are more sensitive to small-order changes in the object morphology ( $V \propto \nu^2$ ,  $\Phi \propto \nu^3$ ; see Lachaume 2003).

**Table 1.** Calibrator star information.

Star	$V$	$K$	Spectral type	$d_{\text{UD}}$ [mas]
HD 108570	6.14	4.12	K1III	$0.72 \pm 0.05$ <sup>(a)</sup>
HD 101328	7.44	3.75	K4III	$1.00 \pm 0.01$ <sup>(b)</sup>
HD 104479	4.75	3.92	K0III	$0.76 \pm 0.01$ <sup>(a)</sup>
HD 106248	6.35	3.73	K2III	$0.94 \pm 0.01$ <sup>(a)</sup>
HD 111123	1.30	1.98	B0.5IV	$0.84 \pm 0.06$ <sup>(a)</sup>
HD 121384	6.01	4.00	G8V	$0.76 \pm 0.05$ <sup>(a)</sup>
HD 135452	6.88	3.43	K3III	$1.13 \pm 0.02$ <sup>(a)</sup>
HD 145921	6.15	3.62	K2III	$0.96 \pm 0.01$ <sup>(b)</sup>
HD 152534	6.77	4.54	G8III	$0.60 \pm 0.04$ <sup>(a)</sup>
HD 170499	7.76	3.05	K4III	$1.24 \pm 0.02$ <sup>(b)</sup>
HD 174631	6.11	2.94	K1III	$1.25 \pm 0.02$ <sup>(b)</sup>
HD 177756	3.43	3.56	B9V	$0.53 \pm 0.04$ <sup>(a)</sup>
HD 181110	7.30	3.71	K3III	$0.95 \pm 0.01$ <sup>(b)</sup>
HD 183925	6.75	2.92	K5III	$1.44 \pm 0.02$ <sup>(a)</sup>

Notes. The  $V$ -band magnitudes were taken from SIMBAD and the  $K$ -band magnitudes from the 2MASS point source catalog. References. <sup>(a)</sup> UD diameter computed with ASPRO. <sup>(b)</sup> UD diameter determined with the ESO CalVin tool.

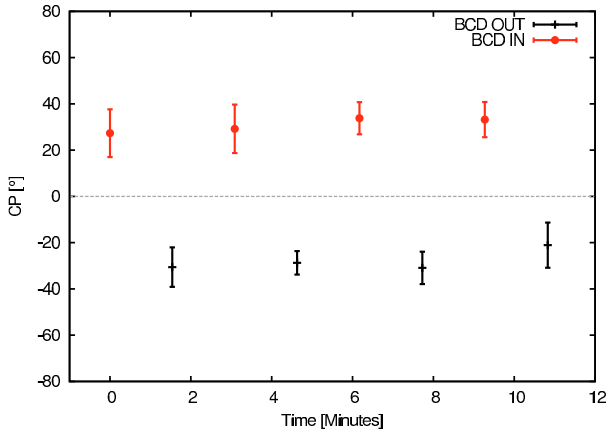


**Fig. 3.** Closure phases recorded on 2008-06-02 on R CrA in the  $K$ -band using the AMBER beam commutation device (BCD), showing the expected CP sign change between BCD OUT (black) and BCD IN (red).

#### 4. Modeling

In this section we describe the geometric and physical models which we fitted to our interferometric data to constrain the spatial distribution of the circumstellar material around R CrA. Besides circumstellar dust and gas emission, the  $K$ -band might contain flux contributions from the stellar photosphere. Therefore we estimate the photospheric flux contributions by comparing the de-reddened SED of R CrA with atmospheric models (Fig. 12), yielding relatively small values between  $\sim 0.5\%$  (assuming the spectral type F5, Garcia Lopez et al. 2006) and  $\sim 3\%$  (spectral type B8, Bibo et al. 1992) of the total flux for the  $K$ -band. Given this result, it seems justified to neglect the photospheric contributions and to include only the thermal emission of hot circumstellar material in our modeling process (with the exception of the curved rim model, see Sect. 4.6).

In order to fit the described models to our interferometric data, we first generate model images for each model and each set of parameters. By construction, the geometric models (Sects. 4.1 to 4.5) are monochromatic, while for our curved rim model (Sect. 4.6), we compute the brightness distribution for each spectral channel separately, assuming the computed surface layer

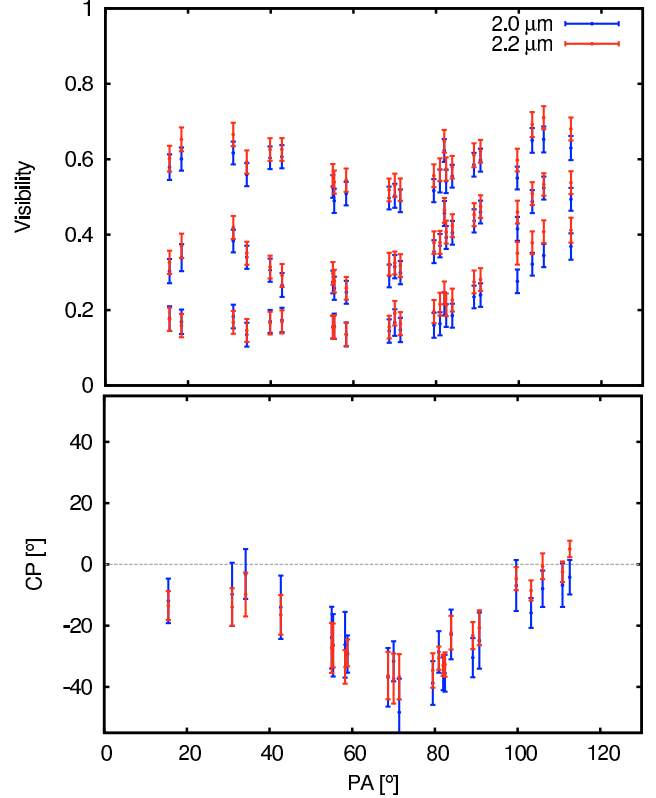


**Fig. 4.** Visibilities (*top*) and closure phases (*bottom*) measured for R CrA with the E0-G0-H0 telescope configuration towards different position angles and for two representative spectral bands around  $\lambda = 2.0 \mu\text{m}$  ( $1.96\text{--}2.04 \mu\text{m}$ ) and  $2.2 \mu\text{m}$  ( $2.16\text{--}2.24 \mu\text{m}$ ). In both cases, three spectral channels around the central wavelength were averaged.

temperature for each disk annulus. From these model images (with a scale of  $0.2 \text{ mas/pixel}$ ), we compute the Fourier amplitudes (visibilities) and Fourier phases for the  $uv$ -coordinates covered by the interferometric observations. Model visibilities  $V'$  and closure phases  $\Phi'$  are computed for each spectral channel separately and then compared to the observables ( $V, \Phi$ ) and their uncertainties ( $\sigma_V, \sigma_\Phi$ ) by adopting  $\chi_r^2 = \chi_{r,V}^2 + \chi_{r,\Phi}^2$  as the likelihood estimator, with

$$\chi_{r,V}^2 = \frac{1}{N_V} \sum_{i=1 \dots N_V} \left[ \left( \frac{V_i - V'_i}{\sigma_{V_i}} \right)^2 \right] \quad (1)$$

$$\chi_{r,\Phi}^2 = \frac{1}{N_\Phi} \sum_{i=1 \dots N_\Phi} \left[ \left( \frac{\Phi_i - \Phi'_i}{\sigma_{\Phi_i}} \right)^2 \right], \quad (2)$$

where  $N_V$  and  $N_\Phi$  are the degrees of freedom for the individual visibility and closure phase measurements, respectively. In order to find the best-fit set of parameters for each model, we vary all free parameters on a parameter grid and search for the global  $\chi_r^2$  minimum.

In the following, we give a detailed description of the applied models and show the obtained best-fit results for the spectral channel around  $2.2 \mu\text{m}$  (Figs. 5 to 12). A comparison between the model and the data obtained in all spectral channels is shown in Figs. 13 and 14. The derived best-fit parameters are given in Table 2.

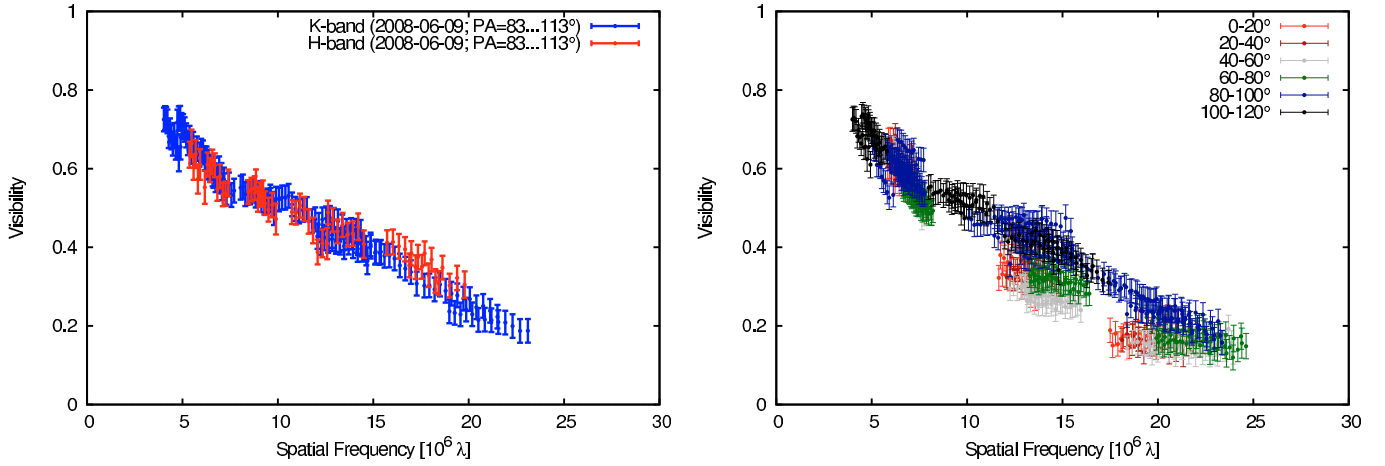


**Fig. 5.** *Left:* visibilities derived from four R CrA observations taken on 2008-06-09 and covering the PA range between 83° and 113°. For the *H*- and *K*-band spectral channels covered by our observations, the measured visibilities follow practically an identical visibility profile. *Right:* comparing the visibility measured during four observing nights towards very different position angles (coded with different colors) reveals a strong position angle dependence of the visibility function, in particular at spatial frequencies above  $8 \times 10^6 \lambda$ .

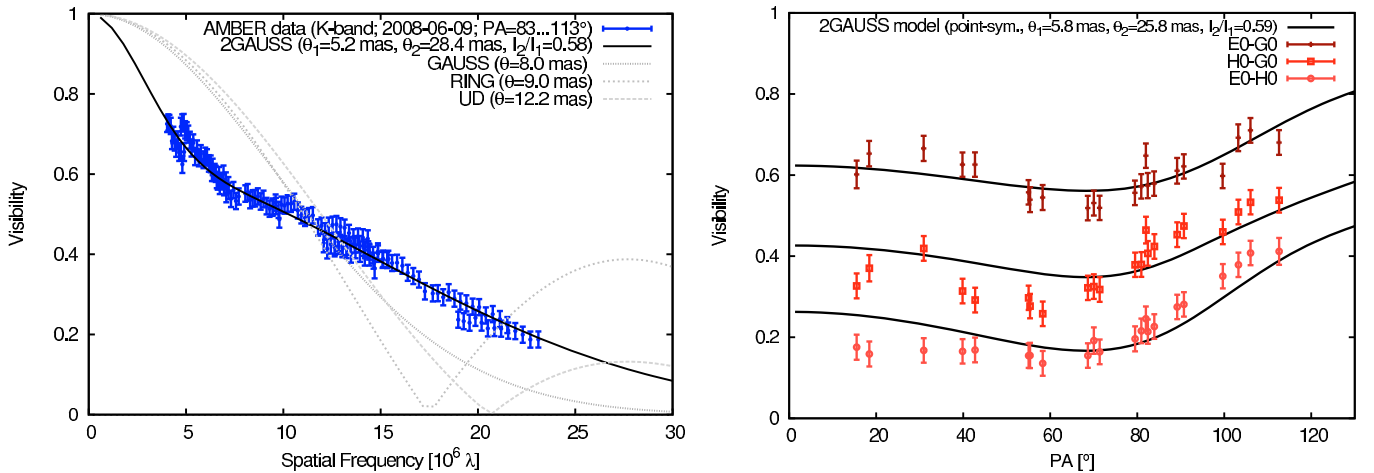


**Fig. 6.** *Left:* comparison of the *K*-band visibilities measured for the PA range 83–113° with various point-symmetric model geometries. It is evident that one-component models, such as UD, RING, and GAUSS geometries, are not consistent with the visibility profile, while a point-symmetric two-component Gaussian model (2-GAUSS) can reproduce the visibilities reasonably well, possibly indicating the presence of two spatial components such as an envelope and a disk (Sect. 4.2). *Right:* fitting the 2-GAUSS model to the visibility data measured towards very different PAs shows that this model cannot reproduce the measured position angle dependence of the visibilities, in particular on the longer baselines.

#### 4.1. UD, RING, GAUSS: point-symmetric models

For a first quantitative interpretation of our data, we employed the commonly used uniform disk (UD), ring (RING), and Gaussian (GAUSS) geometries. By construction, these simple geometries are point-symmetric and, thus, not able to reproduce any object elongation or object asymmetries. Therefore, in contrast to the following Sects. 4.3 to 4.6, here we aim only at reproducing the measured visibilities, being aware that the real object geometry is, in fact, not point-symmetric. Nevertheless, these simple models can be useful to estimate the characteristic size  $\theta$  of the source brightness distribution and to allow a comparison with interferometric studies of other objects. In order to minimize potential influences from object elongation, we applied these model fits to a data subset, covering a smaller PA range. Due to the large number of available independent measurements, we have selected the PA interval 83–113°. From the obtained best-fits (grey curves in Fig. 6, left) it is evident that

neither of these point-symmetric standard geometries can reproduce the measured visibilities.

#### 4.2. 2-GAUSS: indications for a disk+envelope geometry

A plausible explanation for the detected strong deviations between standard model geometries and the measured visibilities might be the presence of multiple components, such as a disk and an envelope component. This scenario also gains support from earlier studies which required the presence of a particularly massive circumstellar envelope (Natta et al. 1993) to reproduce the SED of R CrA.

As a simple two-component geometry, we considered a model which consists of two Gaussian components. In a first attempt (model 2-GAUSS), we fixed the center of the two Gaussians and varied only their *FWHM* diameter ( $\theta_1$ ,  $\theta_2$ ) and intensity ratio ( $I_2/I_1$ ), which allows us to reproduce the

**Table 2.** Model-fitting results.

Model	Compact component									Extended component		Goodness-of-fit		
	$\theta_1$ [mas]	$f$	$\rho$ [mas]	$\phi^{(a)}$ [ $^\circ$ ]	$i$ [ $^\circ$ ]	$s$	$R$ [AU]	$H/R$	$\epsilon$	$\theta_2$ [mas]	$I_2/I_1$	$\chi_{r,V}^2$	$\chi_{r,\Phi}^2$	$\chi_r^2$
<b>Point-symmetric models:</b>														
UD	13.86											24.82	29.32 <sup>(c)</sup>	25.92
RING	8.92	0.25 <sup>(b)</sup>										26.38	29.32 <sup>(c)</sup>	25.21
GAUSS	8.55											18.16	29.32 <sup>(c)</sup>	20.88
2-GAUSS	5.77									25.78	0.59	2.35	29.32 <sup>(c)</sup>	8.92
<b>Asymmetric models:</b>														
BINARY	4.8		6.2	34						14.8	1.04	3.47	5.32	3.93
SKEWED RING		0.8		190	14	0.64	0.44			27	0.58	1.58	3.13	1.96
VERTICAL RIM				132	16		0.60	0.35		27	0.68	2.30	6.16	3.25
CURVED RIM				180	35				$\epsilon_{cr}$	32	0.50	1.77	3.28	2.14

Notes. <sup>(a)</sup> This column gives the model orientation, measured East of North. For the BINARY model,  $\phi$  gives the PA of the separation vector, while for the SKEWED RING, VERTICAL RIM, and CURVED RIM models, the orientation of the ellipse/rim major axis is given. Due to a lack of closure phase calibration observations on the E0-G0-H0 array configuration, we are unfortunately not able to unambiguously define the CP sign, resulting in a 180°-ambiguity in the derived position angles. <sup>(b)</sup> In the fitting process, this parameter was fixed. <sup>(c)</sup> This model is point-symmetric, resulting in a CP which is identical zero.

visibility profile measured towards a narrow PA-range reasonably well (Fig. 6, left). The parameters of this two-Gaussian model (model 2-GAUSS) are listed in Table 2. Of course, being point-symmetric, the model cannot reproduce the measured non-zero closure phases. However, the model allows one to explain the pronounced change of slope, which can be seen in the visibility function around spatial frequency  $\nu \sim 8 \times 10^6 \lambda$ . At shorter spatial frequencies, the measured visibilities do not show any significant position angle dependence, while at higher spatial frequencies, the visibilities differ significantly toward different position angles (see Fig. 5, right). This strongly suggests the presence of at least two spatial components, one being rather extended and point-symmetric (dominating at  $\nu \lesssim 8 \times 10^6 \lambda$ ) and the other being more compact and strongly asymmetric (and dominating at  $\nu \gtrsim 8 \times 10^6 \lambda$ ). Based on this rather general argument, we include two spatial components in all model geometries, namely

- (a) an extended, symmetric component, which we represent with a Gaussian (in the following, this component will be referred to as “Envelope”) and;
- (b) a compact, elongated, and asymmetric component (in the following referred to as “Disk”), which has the purpose of reproducing the measured non-zero closure phases and the detected position angle dependence of the interferometric observables.

Of course, for our modeling, the two components only represent geometric quantities on different spatial scales, and their denotation as “Envelope” and “Disk” is, at the modeling stage, done only for the sake of clarity. Therefore, we include in all following models (with the exception of the 2-GAUSS and BINARY model, which consist of two Gaussian components itself) an envelope component, which is represented by two free parameters, namely the FWHM diameter ( $\theta_2$ ) and the envelope/disk flux ratio ( $I_2/I_1$ ).

#### 4.3. BINARY: asymmetric two-component Gaussian model

The presence of close companions can introduce strong asymmetries in the source brightness distribution and might cause strong non-zero closure phases such as those detected in our VLTI/AMBER measurements. For R CrA, this interpretation

seems particularly appealing, since two earlier studies proposed the presence of multiple stellar sources to explain the measured spectro-polarimetric signatures (Takami et al. 2003) and the unexpected hard X-ray emission (Forbrich et al. 2006). From their spectro-astrometric signal, Takami et al. (2003) derived a lower limit of 8 AU ( $\geq 60$  mas) for the apparent separation of this hypothetical companion. Given this wide separation, the binary should be clearly detectable in our AMBER data. As illustrated in Fig. 3 of Kraus et al. (2009), binaries with such a wide separation cause a high-frequency cosine modulation in the wavelength-differential visibilities and closure phases (this argument holds as long as the separation is large compared to the diameter of the individual components). Neither the measured visibilities nor closure phases show such a systematic, wavelength-differential modulation (Figs. 13 and 14), which clearly indicates that no companion with a separation  $\rho \gtrsim 20$  mas is significantly contributing to the near-infrared emission. In order to investigate up to which flux ratio  $q = I_{comp}/I_{total}$  our observations would be sensitive to the presence of such a hypothetical companion star, we simulated the K-band wavelength-differential signatures of a compact companion star around a point-symmetric, extended component such as derived in Sect. 4.2 and compare the amplitude of the predicted wavelength-differential modulations with the achieved differential visibility and CP accuracy. Based on these simulations (Fig. 7), we estimate that our observations rule out the existence of a companion star for the separation range  $20 \text{ mas} \leq \rho \leq 200 \text{ mas}$  and for K-band flux ratios brighter than  $\sim 1:40$ . The upper limit in this separation range is given by the field-of-view of the used VLTI/AT telescopes. Besides these constraints from VLTI/AMBER interferometry, we obtained bispectrum-speckle interferometric observations with the ESO 3.6 m telescope (H-band; data from 2007-04-24 and 2007-04-27) using the Rockwell HAWAII detector of our visitor speckle camera. For image reconstruction we used the bispectrum speckle interferometry method (Weigelt 1977; Weigelt & Wirtitzer 1983; Lohmann et al. 1983). Both the derived power-spectrum and the reconstructed diffraction-limited bispectrum speckle image (Fig. 8), shows R CrA as a point-source, ruling out the existence of a companion star at separations  $\rho \gtrsim 60$  mas, down to a flux ratio of 1:40.

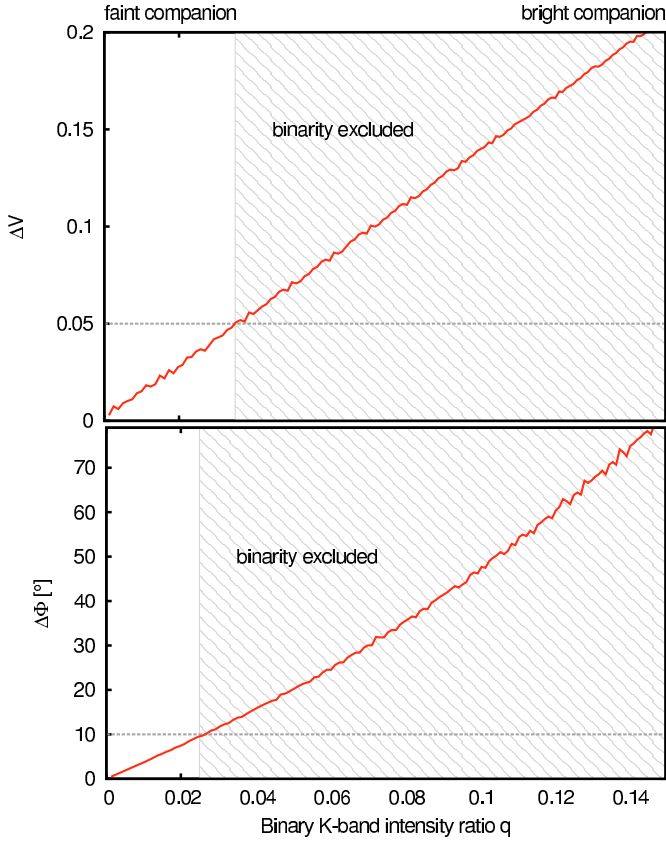


**Fig. 7.** Simulation of the expected visibility (*top*) and closure phase (*bottom*) signatures of a hypothetical companion star, plotted as function of the binary flux ratio. For these simulations, we assume a point-symmetric extended component (for which we use the 2-GAUSS geometry discussed in Sect. 4.2) and add a compact companion at a separation of 60 mas, corresponding to the minimum separation of the proposed wide-separation companion star (Takami et al. 2003). Then, we compute the residuals between the model with and without companion star and measure the amplitude of the wavelength-differential visibility and CP modulation for the *K*-band spectral window. The dashed horizontal lines give the achieved wavelength-differential visibility and closure phase accuracy, indicating that our observations should be sensitive to any companion star contributing more than  $q = 1:40$  of the total flux (shaded area).

In order to test for the presence of a companion at shorter separation, we also fitted a binary star model to our AMBER data. Since it is likely that the near-infrared emission of the two components is not dominated by photospheric emission, but instead by the thermal emission of hot circumstellar material, we represent the two components not with point-sources, but with extended geometries, namely Gaussians. The choice of this geometry is motivated by our results from Sect. 4.2, where we showed that two Gaussians are well suited to represent the radial intensity profile towards some PA ranges.

In this model, the free parameters are the *FWHM* sizes of the two Gaussians ( $\theta_1, \theta_2$ ), their flux ratio ( $I_2/I_1$ ), their angular separation ( $\rho$ ), and the position angle ( $\phi$ ). As shown in Fig. 9, the best-fit binary model can provide only a moderate fit to the measured visibilities and CPs ( $\chi_r^2 = 3.93$ ). Furthermore, as will be discussed in Sect. 5.2, the found best-fit solution is not physically meaningful in the context of a companion star scenario.

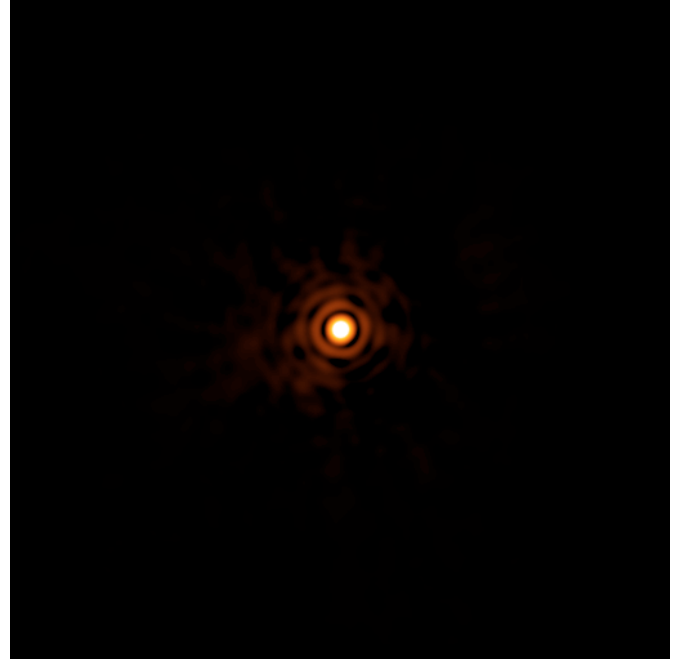


**Fig. 8.** Bispectrum speckle image reconstructed from *H*-band speckle interferograms recorded with the ESO 3.6 m telescope on 2007-04-24 (field-of-view 6"). At the achieved diffraction-limited angular resolution of 95 mas, R CrA appears as a point-source. The first and second diffraction ring are clearly visible with noise-features on the 1%-level, allowing us to rule out the existence of a companion star in this separation/brightness contrast range.

#### 4.4. SKEWED RING model

For passive irradiated disks, most of the near-infrared emission should emerge from hot dust located in a narrow annulus around the dust sublimation radius. Therefore, Monnier & Millan-Gabet (2002) and others have argued that ring geometries might provide a good approximation for the appearance of YSO disks on AU-scales. While for face-on disks, point-symmetric rings seem appropriate, ring models are likely to be an over-simplification for disks seen under significant inclination. Since one side of the rim should appear brighter than the other, Monnier et al. (2006) proposed a simple mathematical modification of the standard ring model using a sinusoidal modulation of the ring brightness as a function of the azimuthal angle. We apply a similar modeling approach using the intensity distribution

$$I(r, \alpha) = (1 - s \cdot \sin(\alpha - \phi)) \cdot \exp\left(-\frac{4 \ln 2 \cdot (r - pR)^2}{(fpR)^2}\right), \quad (3)$$

where the first term modulates the brightness distribution as a Gaussian centered at radius  $R$  and of fraction width  $f$  (*FWHM*). The brightness distribution  $I(r, \alpha)$  is defined in a polar coordinate system, where  $r$  denotes the radius from the center and  $\alpha$  the azimuth angle. The projection factor  $p$  can be used to take inclination effects into account and is given by

$$p = \cos i \left( \cos^2 i \cdot \cos^2(\alpha - \phi) + \sin^2(\alpha - \phi) \right)^{-1/2}. \quad (4)$$

In both equations,  $\phi$  denotes the PA along which the major axis of the apparent disk ellipse is aligned. The fitted free parameters are the ring radius ( $R$ ), the fractional ring width  $f$ , the position angle  $\phi$ , the inclination  $i$ , the skew parameter  $s$ , as well as the two envelope parameters ( $\theta_2, I_2/I_1$ ) described above. For this skewed ring model, our fitting algorithm can reach good agreement with the data ( $\chi_r^2 = 1.96$ ; Fig. 10).

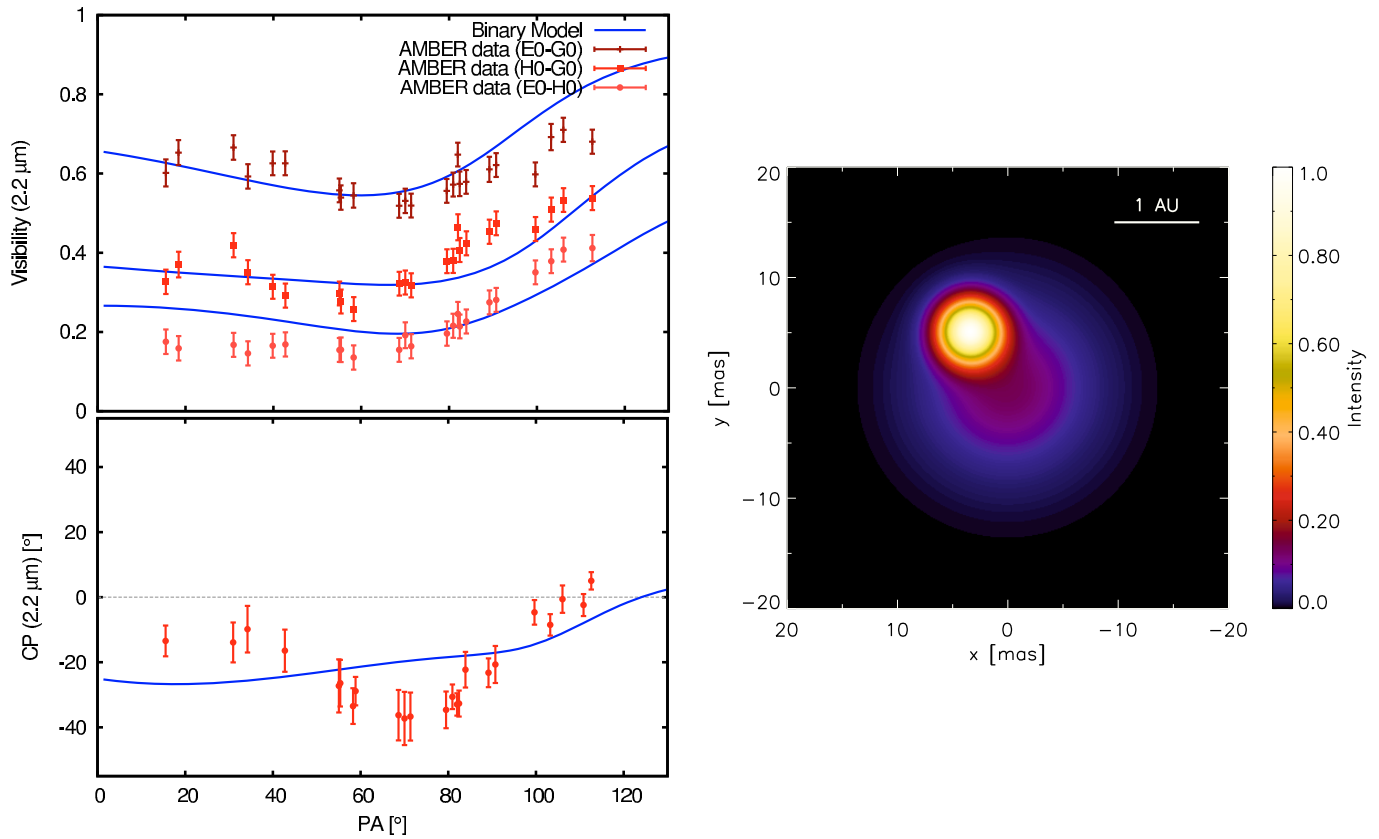


**Fig. 9.** *Left:* comparison between the AMBER observables and the model visibilities (*top*) and closure phases (*bottom*) from our BINARY model. *Right:* image corresponding to our best-fit model.

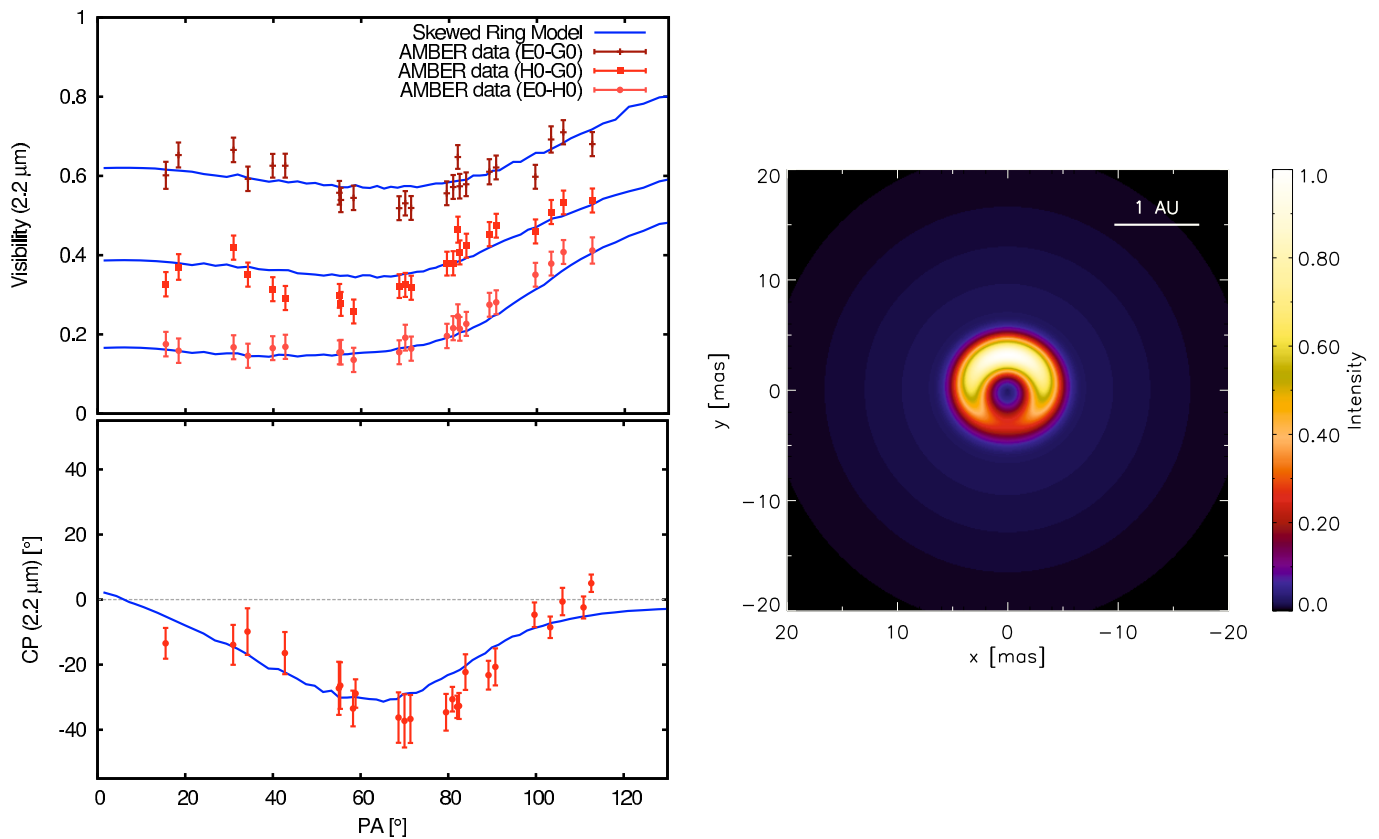


**Fig. 10.** *Left:* comparison between the AMBER observables and the model visibilities (*top*) and closure phases (*bottom*) from our SKEWED RING model. *Right:* image corresponding to our best-fit model.

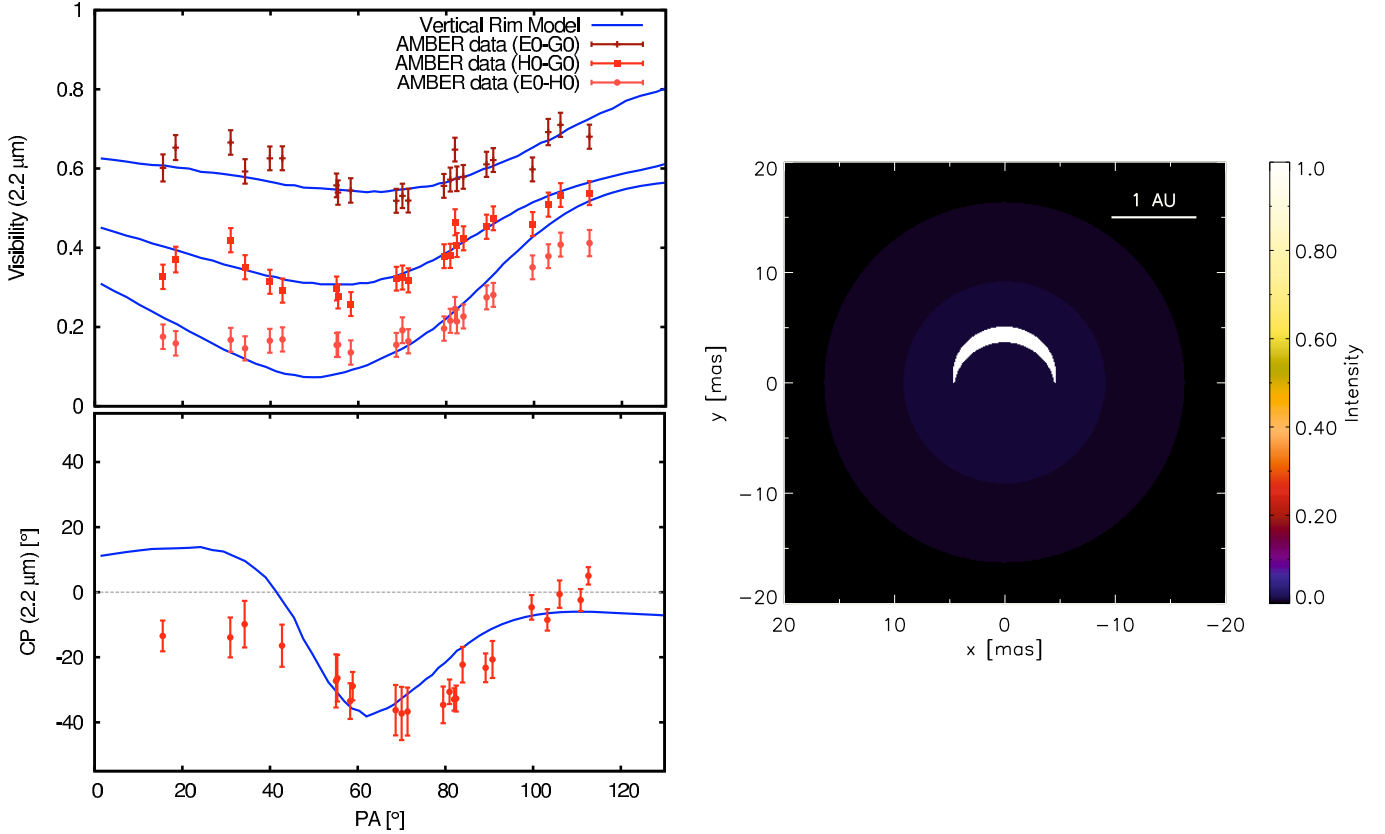


**Fig. 11.** *Left:* comparison between the AMBER observables and the model visibilities (*top*) and closure phases (*bottom*) from our VERTICAL RIM model. *Right:* image corresponding to our best-fit model.

#### 4.5. VERTICAL RIM model

Over the last decade, detailed physical models have been developed to describe the 3D structure of the inner dust rim around Herbig Ae stars. Dullemond et al. (2001) provided a first mathematical description of the inner rim geometry and considered a perfectly vertical inner rim. Since a vertical rim should result in very strong asymmetries, it seems promising to test whether such a model can explain the strong closure phases detected in our R CrA data. To compute the brightness distribution, we assume that all near-infrared flux emerges from the hot, illuminated rim surface. In this model, the free parameters are the rim radius  $R$ , the rim scale height  $H/R$ , the position angle  $\phi$ , the system inclination  $i$ , and the envelope parameters  $\theta_2$  and  $I_2/I_1$ . Our resulting best fit is shown in Fig. 11, but provides no satisfactory representation of the data ( $\chi_r^2 = 3.25$ ).

#### 4.6. CURVED RIM model

Following the pioneering work by Natta et al. (2001) and Dullemond et al. (2001), several studies aimed to refine the theoretical description of the rim geometry. For instance, IN05 pointed out that the dust sublimation temperature should depend on the local gas density. Accordingly, the dust sublimation temperature should be highest in the disk midplane and decrease with scale height  $H$ , resulting in a curved shape of the inner rim. In order to further increase the physical accuracy, Tannirkulam et al. (2007) included the effect of dust grain sedimentation, showing that the presence of a population of small and large dust grains results in an even stronger rim curvature than predicted by the IN05 model.

To compute the radial dependence of the scale height of the disk photospheric layer  $H/R$ , we follow the analytical approach by IN05. The dependence of the dust sublimation temperature on the local gas density  $\rho_g$  (in  $\text{g}/\text{cm}^3$ ) is described by the relation from Pollack et al. (1994), namely  $T_{\text{subl}} = 2000 \text{ K} \cdot \rho_g^{0.0195}$ . In order to avoid unrealistic cutoffs at the outer edge of the puffed-up inner rim, we include the more extended disk regions in our model as well and construct our disk with the following components:

- (a) *Puffed-up inner rim:* this region extends from  $R_{\text{subl}}$  to the point where the rim surface layer becomes optically thin to the stellar radiation.
- (b) *Shadowed region:* entering the optically thin regime, the rim can no longer maintain its puffed-up shape and the scale height decreases as  $d(H/R)/dR = -1/(8R)$ , as derived by Dullemond et al. (2001).
- (c) *Flared outer disk:* at larger radii, the disk might enter a flared shape, which we parameterize with  $H/R = H_0 (R/R_0)^{9/8}$  and  $T(R) \propto R^{-3/4}$  (Kenyon & Hartmann 1987).

In addition, the model includes the photospheric emission, which we estimate from the SED by comparing the stellar flux with the measured near-infrared flux. Please note that our near-infrared observations are mainly sensitive to regions (a) and (b), while the parameters for the outer flared disk region are not constrained by our model fits. Therefore, we fixed the parameters  $H_0$  and  $R_0$  to the typical values of  $H_0 = 0.1 \text{ AU}$  and  $R_0 = 10 \text{ AU}$ . As total disk mass, we assume  $M_{\text{disk}} = 0.012 M_{\odot}$  (Groppi et al. 2007) with a standard gas-to-dust ratio of 100:1. Besides the luminosity  $L$  which is incident on the disk rim, the most sensitive parameter in the IN05 model is  $\epsilon$ . This variable is defined as the

ratio of the Planck mean opacity at the dust evaporation temperature  $T_{\text{subl}}$  to the Planck mean opacity at the stellar effective temperature  $T_{\star}$  and defines the cooling efficiency of the dust grains. It therefore depends on the precise dust chemistry and grain size distribution. For a given grain population,  $\epsilon$  typically increases for larger grain sizes, moving the rim location closer to the star (see IN05). Above a certain threshold ( $\epsilon \gtrsim \epsilon_{\text{cr}} = 1/\sqrt{3}$ ), the location of the optically thick dust rim stays nearly constant, and the largest grains can only survive closer to the star in an optically thin regime. Therefore, we imposed for our fit that  $\epsilon$  cannot exceed  $\epsilon_{\text{cr}}$ . In addition, the model assumes that absorption and continuum emission by gas inside the dust sublimation radius is negligible. This assumption is supported by the theoretical work of Muzerolle et al. (2004), who found that for the accretion rate of R CrA ( $\dot{M}_{\text{acc}} = 10^{-7.12} M_{\odot}/\text{yr}$ , Garcia Lopez et al. 2006), the gas located inside the dust sublimation radius should be optically thin.

After computing the disk scale height  $H(r)$  and blackbody temperature  $T(r)$  for each disk annulus, we construct synthetic images of the disk brightness distribution. By computing these images for each spectral channel separately, we can simulate the wavelength-differential changes resulting from the disk temperature distribution.

The free disk model fitting parameters are the position angle  $\phi$ , the system inclination  $i$ , the grain cooling efficiency  $\epsilon$ , and the envelope parameters  $\theta_2$  and  $I_2/I_1$ . Of course, another crucial parameter is the luminosity  $L$ , which is heating the inner dust rim, and which might contain stellar light contributions ( $L_{\star}$ ) as well as contributions due to active accretion ( $L_{\text{acc}}$ ). Although the precise amount of either of these contributions is still not well known, it is likely that the total incident luminosity  $L := L_{\star} + L_{\text{acc}}$  is neither as low as  $\sim 2 L_{\odot}$  (corresponding to the stellar luminosity of a F5 star, nor that the full bolometric luminosity of  $\sim 99 L_{\odot}$  (Bibo et al. 1992) derived from KAO photometry can be solely attributed to this single source. Therefore, we treat  $L$  as a free parameter and keep the other stellar parameters, which have a less significant influence on our modeling results, fixed to the values corresponding to a B8-type star ( $T_{\text{eff}} = 12\,000\text{ K}$ ,  $M_{\star} = 3.0 M_{\odot}$ , Bibo et al. 1992). Then, we adjust the absorption coefficient  $A_V$  to roughly reproduce the SED of R CrA at UV/visual wavelengths. Following Bibo et al. (1992), the total-to-selective extinction ratio  $R_V$  was fixed to 4.7. In order to include the emission of the puffed-up inner rim in our model SED, we follow the approach outlined by IN05, assuming that the rim surface layer reprocesses the incident light and re-emits it as a blackbody of temperature  $\sim 1400\text{ K}$ . When modeling the SED of R CrA, one faces the general problem that the visual/near-infrared emission also contains major scattered flux contributions from the circumstellar envelope, as described in Sects. 4.2 and 5.1. Due to this strong ‘‘contamination’’, we decided not to include the SED as an additional modeling constraint, but to treat the fraction of stellar luminosity which is reprocessed at near-infrared wavelengths  $\beta := L_{\text{NIR}}/L$  as a free model parameter, which is adjusted to match the measured SED of R CrA. In Sect. 5.3, we will compare the derived  $\beta$ -value with the predictions from the IN05 model and discuss the consistency between the measured SED and the puffed-up inner rim scenario.

Using our modeling approach, we find that the parameter combination  $L = 29 L_{\odot}$  and  $\epsilon = \epsilon_{\text{cr}}$  is able to simultaneously reproduce the measured visibilities and closure phases ( $\chi_r^2 = 2.14$ , Fig. 12, top, left) as well as the visual- to near-infrared SED (with  $A_V = 5.0$  and  $\beta = 0.35$ ; see Fig. 12, bottom, left). For the following reasons, both parameters appear to be relatively

well constrained:

- Assuming a higher value for  $L$  would push the dust sublimation radius outwards, resulting in too low visibilities (e.g., for  $L = 50 L_{\odot}$ , the best-fit  $\chi_r^2$ -value increases already to 2.85).
- A lower luminosity would require to increase  $\beta$  above physically reasonable values (e.g., for  $L = 20 L_{\odot}$ , already more than 60% of the stellar light would have to be reprocessed by the inner rim).
- $\epsilon$ -values significantly lower than  $\epsilon_{\text{cr}}$  seem to be excluded, since this would again result either in too low visibilities, or require to increase  $\beta$  substantially.

We conclude, that already with a relatively small number of free parameters ( $L$ ,  $\epsilon$ ,  $\phi$ ,  $i$ ,  $\theta_2$ ,  $I_2/I_1$ ), it is possible to simultaneously reproduce the interferometric observables ( $\chi_r^2 = 2.14$ ) and the relevant parts of the SED. At wavelengths  $\gtrsim 3\ \mu\text{m}$ , our model is not able to reproduce the SED, since we do not include the flux contributions from the more extended disk regions nor from the circumstellar envelope. In Fig. 12 we show the model visibilities and closure phases, the SED, as well as the computed photospheric scale height  $H/R$  and the temperature distribution for our best-fit model. In this model, the inner rim radius is located at 0.38 AU.

## 5. Discussion

### 5.1. Radial intensity profile

As shown in Sect. 4.1, it is evident that the radial intensity profile measured toward R CrA cannot be well represented with simple one-component geometries, such as rings. Instead, the visibility function has an approximately linear slope (Fig. 5, left), showing remarkable similarities with the visibility profile measured by Acke et al. (2008) on the much more massive YSO MWC 297. In both cases, the visibilities could be approximated reasonably well with two Gaussian components. For the case of R CrA, we interpret this finding with the presence of an extended optically thin envelope, which contributes about one-third of the total  $K$ -band flux, likely through scattered light. This extended emission might represent scattered light from an optically thin spherical halo or from the walls of an associated outflow cavity. The presence of an envelope around R CrA was already deduced earlier from SED fits (Natta et al. 1993) and from polarimetric observations (Clark et al. 2000) and seems in line with the early evolutionary stage of the object.

Independent of the precise physical interpretation of the measured visibility profile, our finding shows that the commonly applied ring model fits often represent an over-simplification of the complex environment around YSOs. Since these ring fits are commonly applied to single-baseline, broad-band interferometric observations, the uncertainties of the real underlying radial intensity profile likely contribute significantly to the scatter which is observed in size-luminosity diagrams (Monnier et al. 2005). Therefore, very detailed interferometric studies on some additional sources will be essential to identify the real underlying source structure and will have a direct impact on the proper interpretation of the data obtained in survey-type observations.

### 5.2. Non-detection of the proposed binary companion

Given the earlier speculations about the existence of a companion star for R CrA (Takami et al. 2003; Forbrich et al. 2006, see discussion in Sect. 2), it is an important result that we did not

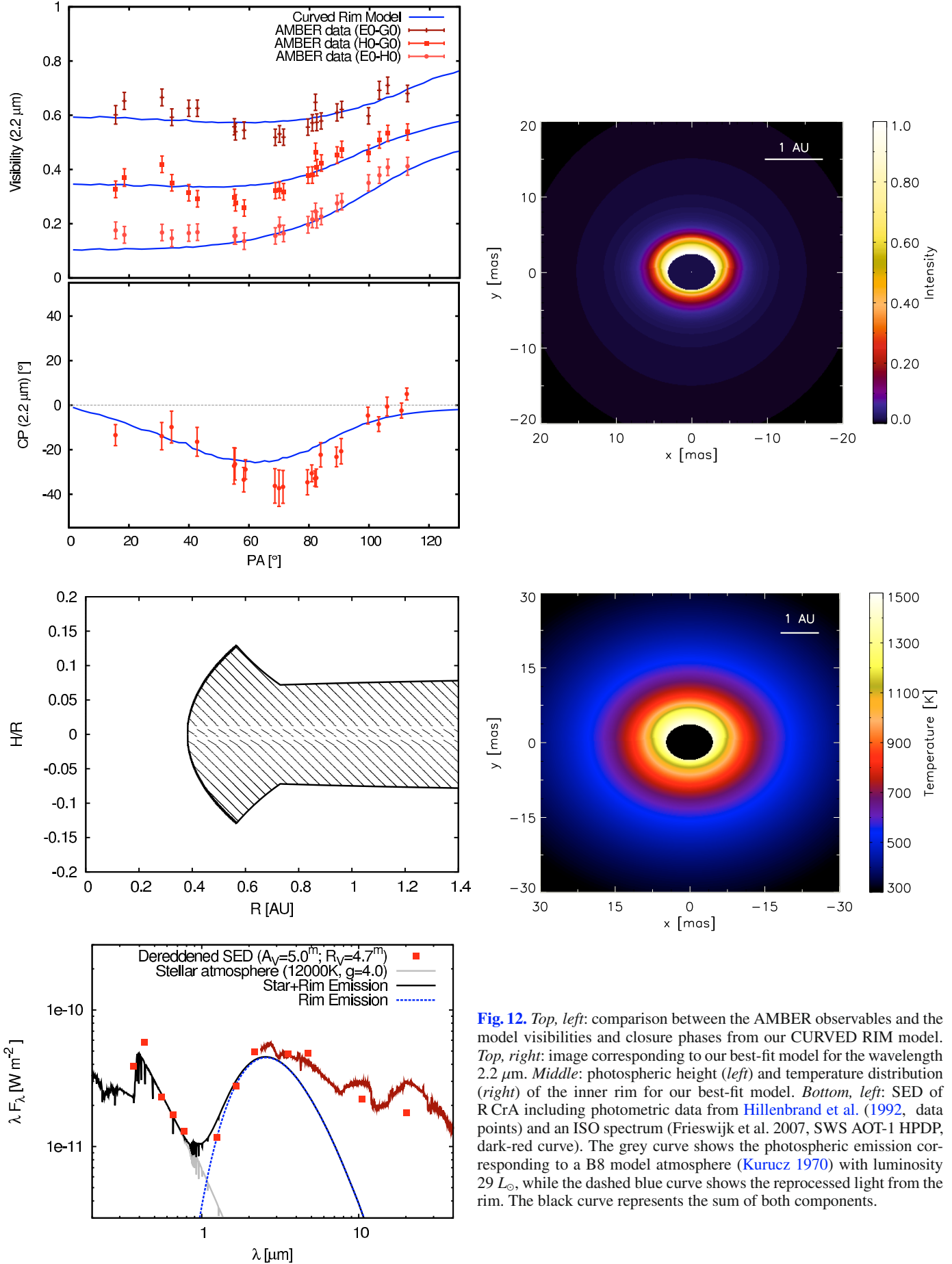


**Fig. 12.** *Top, left:* comparison between the AMBER observables and the model visibilities and closure phases from our CURVED RIM model. *Top, right:* image corresponding to our best-fit model for the wavelength  $2.2 \mu\text{m}$ . *Middle, left:* photospheric height (*left*) and temperature distribution (*right*) of the inner rim for our best-fit model. *Bottom, left:* SED of R CrA including photometric data from Hillenbrand et al. (1992, data points) and an ISO spectrum (Frieswijk et al. 2007, SWS AOT-1 HPDP, dark-red curve). The grey curve shows the photospheric emission corresponding to a B8 model atmosphere (Kurucz 1970) with luminosity  $29 L_\odot$ , while the dashed blue curve shows the reprocessed light from the rim. The black curve represents the sum of both components.

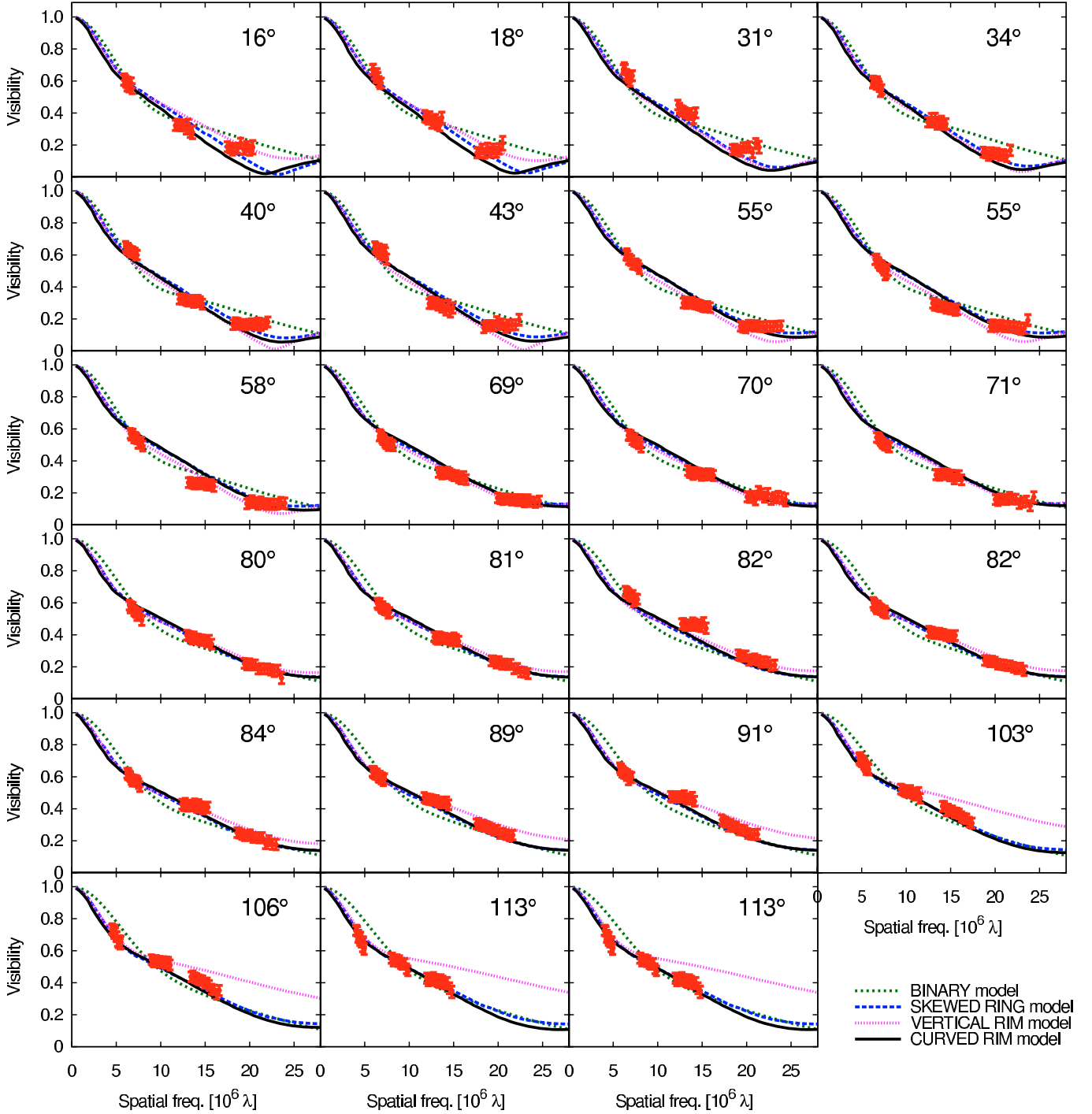


**Fig. 13.** Comparison of the measured wavelength-dependent AMBER visibilities and the model visibilities corresponding to the best-fit model assuming our BINARY model (Sect. 4.3), SKEWED RING model (Sect. 4.4), VERTICAL RIM model (Sect. 4.5), and CURVED RIM model (Sect. 4.6).

find indications for binarity of R CrA from our study. As discussed in Sect. 4.3, it is possible to rule out the presence of wide separation binaries ( $\rho \gtrsim 40$  mas) with rather general arguments. To probe for binaries with smaller separation, we constructed geometric models, which also take into account that each star might be associated with a circumstellar disk (represented by Gaussians in our model). Since this model provided only a poor representation of our data, we consider such a close binary scenario rather unlikely. Furthermore, the best-fit parameters of the binary model do not correspond to a physical solution, since the

extension of the Gaussian components (1.9 and 0.8 AU) exceeds even their projected separation (0.8 AU), resulting in an overlap of the two components. Assuming that the physical separation is of similar order as the projected separation, a hypothetical binary on such small spatial scales would not be stable and would quickly disrupt the circumstellar disks around both components.

Of course, with the existing data, it is difficult to rule out scenarios which might involve three or more spatial components, such as, for instance, a binary system with circumstellar and circumbinary disks. Also, our observations do not rule out the

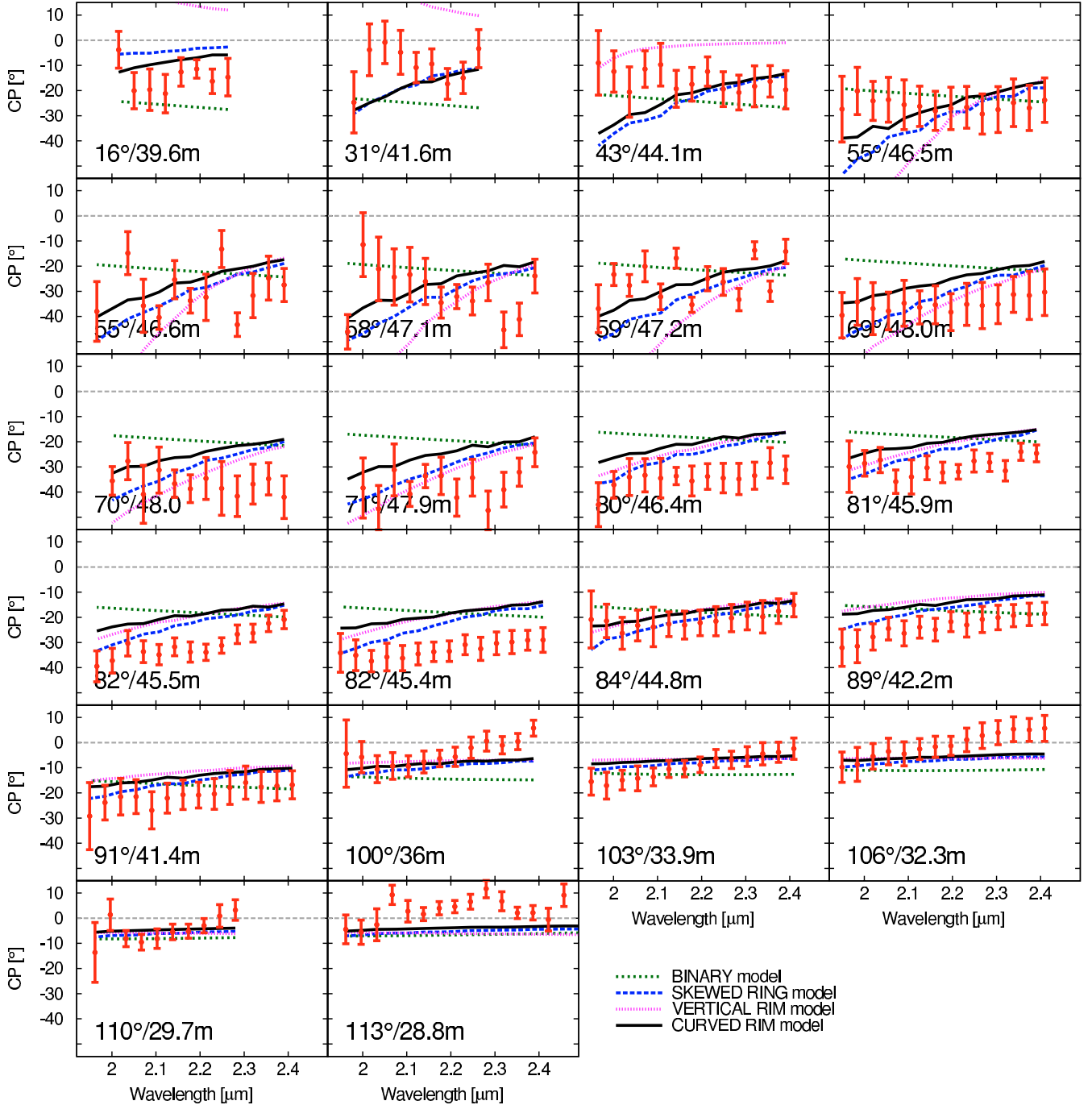


**Fig. 14.** Comparison of the measured wavelength-dependent closure phases with the predictions from our best-fit BINARY model (Sect. 4.3), SKEWED RING model (Sect. 4.4), VERTICAL RIM model (Sect. 4.5), and CURVED RIM model (Sect. 4.6). In each panel, the position angle of the three baselines and the projected length of the longest baseline  $B_{E0-H0}$  is given. Given the equal spacing of the employed linear telescope array, the other two baselines have projected length of  $B_{E0-G0} = B_{E0-H0}/3$  and  $B_{G0-H0} = 2B_{E0-H0}/3$ .

existence of a very deeply embedded companion, which might not contribute significantly to the near-infrared emission. However, this scenario is rather unlikely, since the SED of R CrA peaks in the  $K$ -band (Fig. 12, bottom, left), which makes the existence of an additional strong, far-infrared-emitting component unlikely.

Our non-detection of a binary component around R CrA suggests that the detected hard X-ray emission is not associated with a hypothetical Class I source (Forbrich et al. 2006), but with a single Herbig Ae star. This finding on R CrA is in line with the study by Hamidouche et al. (2008), who concluded from

statistical arguments that the X-ray emissions of Herbig Ae/Be stars have an intrinsic origin. Since neither coronal nor shock-excited X-ray emission is expected for A-type stars, more theoretical work is clearly required in order to identify the X-ray-emitting mechanism of single intermediate-mass pre-main-sequence stars such as R CrA.

### 5.3. Constraints on the rim geometry

Given that our best-fitting results were obtained with the skewed ring model (Sect. 4.4) and the curved rim model (Sect. 4.6), we

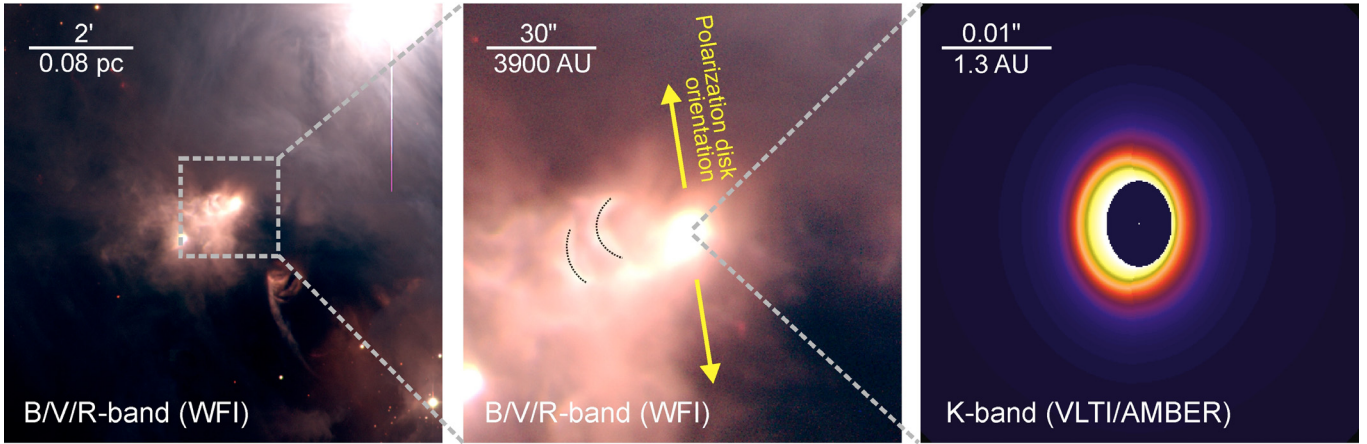


**Fig. 15.** At visual wavelengths the field around R CrA is dominated by the reflection nebula NGC 6729 (*left* panel; color composite: blue: *B*-band, green: *V*-band, red: *R*-band; North is up and east is to the left). Within the reflection nebula, two bow shock-like structures appear (*middle* panel, dashed lines), suggesting an east-western outflow axis, which is roughly perpendicular to the polarization disk reported by [Ward-Thompson et al. \(1985\)](#) and the sub-AU disk resolved by our VLT/AMBER observations (*right* panel; CURVED RIM model image; please note that there is still an 180°-ambiguity in the derived orientation, as discussed in Table 2). The *B/V/R*-band images were taken with the Wide Field Imager (WFI) at the 2.2-m MPG/ESO telescope on La Silla (ESO Press Photo 25a-b/00; image courtesy: European Southern Observatory and F. Comerón).

consider it most likely that our observations are directly tracing the asymmetries introduced by material at the inner truncation radius of the dust disk around R CrA. This interpretation is also supported by the fact that the *H*- and *K*-band visibilities follow within the error bars the same visibility profile (Sect. 3 and Fig. 5, *left*), providing important information about the temperature distribution of the near-infrared emitting disk material. Earlier spectro-interferometric observations on two other Herbig Ae/Be stars ([Kraus et al. 2008](#); [Isella et al. 2008](#)) measured in the *H*-band a significantly higher visibility than in the *K*-band, which was interpreted as the presence of an optically thick, hot gaseous disk component located inside of the dust sublimation radius. For R CrA, we do not measure this visibility increase towards shorter wavelengths, indicating that the disk material in the probed temperature range ( $\gtrsim 1000$  K) is located at similar distances from the star, likely in a narrow region around the dust sublimation radius.

Concerning the detected asymmetries, it is interesting to compare our results with earlier studies on HD 45677 ( $\Phi \lesssim 27^\circ$ , [Monnier et al. 2006](#)) and AB Aur ( $\Phi \lesssim 4^\circ$ , [Millan-Gabet et al. 2006](#)), which also detected asymmetries in the inner region around these Ae- and Be-type stars. Comparing HD 45677 and R CrA, it is remarkable that the closure phases from the two objects could be represented well with a skewed ring model. However, a major difference between both objects concerns the evolutionary stage: HD 45677 is likely an evolved B[e] star, while R CrA is a young, actively accreting Herbig Ae star. Compared to the Herbig Ae star AB Aur, a major difference concerns the physical nature of the asymmetry. For AB Aur, the modeling of [Millan-Gabet et al.](#) showed that the asymmetries around this object originate from a localized region within the disk (maybe a hot accretion spot), while our data seems more consistent with a diffuse structure around the dust sublimation radius. Another Herbig Ae/Be star where strong asymmetries were detected is LkH $\alpha$ 101. Near-infrared aperture-masking observations by [Tuthill et al. \(2001\)](#) revealed a skewed circular structure at a distance of  $\sim 3.4$  AU around this rather massive ( $M_\star \approx 5\text{--}10 M_\odot$ ) and luminous ( $L_\star \approx 480 L_\odot$ ) Herbig Be star. Remarkably, the structure in their observations shows some similarities with our best-fit skewed ring model, which might

suggest that, contrary to earlier suggestions ([Vinković & Jurkić 2007](#)), Herbig Ae and Herbig Be have a common rim structure.

To determine the precise rim shape, we have fitted three different models, namely the skewed ring model (Sect. 4.4), the vertical rim model (Sect. 4.5), and the curved rim model (Sect. 4.6). Formally, the best agreement was found with the geometric skewed ring model ( $\chi_r^2 = 1.96$ ), although it should be noted that the skewed ring model is a purely geometric model and has the largest number of adjustable free parameters (5 disk and 2 envelope parameters). On the other hand, the curved rim model ( $\chi_r^2 = 2.14$ ) has less free parameters (3 disk, 2 envelope, and 1 stellar parameter) and is based on detailed theories about disk structure and dust properties, allowing a direct physical interpretation of the fitted parameters. In this context, the dust cooling efficiency parameter  $\epsilon$  is of particular interest, since this parameter is directly related to the dust properties in the inner disk regions. For instance, [Isella et al. \(2006\)](#) used the curved rim model to derive the maximum dust grain size for a sample of five Herbig Ae/Be stars, finding in all cases relatively large dust grains ( $\gtrsim 0.2 \mu\text{m}$ ). Assuming the same Silicate dust chemistry, we derive for R CrA dust grain sizes larger than  $1.2 \mu\text{m}$  (corresponding to  $\epsilon \gtrsim \epsilon_{\text{cr}}$ ), indicating that the dust in the inner disk regions was already significantly processed by grain growth. In order to reproduce the interferometric data and the SED simultaneously, we require that the incident luminosity, which is heating the inner dust rim, is around  $29 L_\odot$  and that 35% of the stellar light is reprocessed at near-infrared wavelengths. This fraction is somewhat higher than the theoretical value of  $\sim 20\%$  predicted by the IN05 model (see Fig. 4 in IN05). However, this might reflect the fact that a significant fraction of the near-infrared emission is likely not reprocessed light from the inner rim, but scattered light contributions from a circumstellar envelope (Sects. 4.2 and 5.1). Although it is currently unfortunately not possible to properly decompose the disk and envelope SED, it is likely that the  $\beta$ -value has to be corrected by a similar factor as the determined envelope/disk *K*-band flux ratio of 1/3 (Sect. 4.2), which would result in a good agreement with the expected theoretical value. Alternative explanations for the derived high value of  $\beta$  would include an underestimation of the gas disk mass ( $M_{\text{disk}} = 0.012 M_\odot$ ) and the resulting

underestimation of the Silicate sublimation temperature or the presence of highly refractory dust species which sublimate at higher temperature than Silicate grains.

For the derived luminosity of  $\sim 29 L_{\odot}$ , we consider that the dominant contribution is photospheric emission, while the contributions from active accretion are likely less significant, as indicated by the observed low Br $\gamma$ -line luminosity (García López et al. 2006). Accordingly, only about one-third of the total bolometric luminosity ( $\sim 99 L_{\odot}$ , Bibo et al. 1992) can be attributed to R CrA, while the remaining fraction is likely due to contamination from other, more deeply embedded members of the Coronet cluster in the large ( $\sim 45''$ ) field-of-view of the KAO satellite.

For the disk inclination angle, we consider the value determined with the curved rim model ( $i = 35^{\circ}$ ) our most reliable estimate<sup>3</sup> and note that the value is also in good agreement with the inclination angle of  $\sim 40^{\circ}$ , which was derived by Clark et al. (2000) for the reflection nebula NGC 6729 using polarimetric observations. NGC 6729 also shows some remarkable fine-structure, in particular two bow shock-like features (labeled E and F in Clark et al. 2000), which appear east of R CrA (Fig. 15, left and middle). As already suggested by Clark et al., these structures might be created by vigorous, periodic outflow activity from R CrA. The sub-AU scale disk structure resolved by our AMBER observations is oriented approximately perpendicular to these bow shocks ( $\theta = 180, 190^{\circ}$  for the CURVED RIM model and the SKEWED RING model, respectively), suggesting that R CrA is the driving engine which has created these bow shocks (Fig. 15, right). The derived disk orientation is also consistent with the orientation of the polarization disk reported by Ward-Thompson et al. (1985,  $\theta = 189 \pm 5^{\circ}$ ; see Fig. 15, middle). The bright feature extending from R CrA to the south-east (labeled C in Clark et al. 2000) was identified by Clark et al. as scattered light from the walls of a parabolic outflow cavity.

When judging the quality of the obtained fit, it is interesting to note that the IN05 fitting results improved slightly by taking the expected disk temperature gradient effects into account ( $\chi_r^2 = 2.14$ ). For comparison, when we simulate a monochromatic brightness distribution ( $\lambda = 2.2 \mu\text{m}$ ), we yield  $\chi_r^2 = 2.38$ . Nevertheless, with a  $\chi_r^2$ -value of 2.14, the quality of the best fit IN05 model is still relatively poor, indicating that the rim geometry might still not be adequately represented by the employed rim model. Therefore, it will be important to investigate in future studies how the models can be modified to yield a better representation of the measured visibilities and closure phases. For instance, including dust sedimentation and grain growth effects should result in an even more curved rim shape and a broader near-infrared emitting rim region than predicted by the current model (Tannirkulam et al. 2007). Based on the good fitting results obtained with a skewed ring model with a large fractional ring width of 0.8 (Sect. 4.4), we expect that such a modification might improve the visibility/phase fit. Possibly, an improvement could also be obtained by including the optically thin dust condensation zone which is expected to extend inwards of the dust rim, yielding a more diffuse rim structure (Kama et al. 2009). Other very promising modifications concern the presence of multiple grain species, in particular highly refractory metal oxides such as iron or corundum, and a consistent treatment

of backwarming effects. Kama et al. have shown that these effects can move the dust sublimation radius nearly by a factor of 2 closer to the star. With our fitting procedure, this change would result in a higher derived stellar luminosity (i.e. more consistent with the measured bolometric luminosity) and a lower fraction of reprocessed light (i.e. closer to the theoretical expectation). Thus, we expect that these model refinements aim in the right direction in order to further improve the physical consistency of the puffed-up inner rim scenario for R CrA, although a detailed data modeling study will be required in order to test whether the model refinements also affect the rim morphology, as required to yield a better  $\chi^2$ -fit. Finally, one should take into account that our observations probe relatively small physical scales in a highly dynamical and complex environment. Therefore, it cannot be excluded that our interferometric observations might also be affected by local inhomogeneities or astrophysical processes, which are not yet completely included in the employed disk rim models, such as active accretion or the influence of outflow launching on the disk structure.

## 6. Conclusions

We summarize our findings as follows:

- Using 24 VLTI long-baseline interferometric measurements, we studied the near-infrared emission from the Herbig Ae star R CrA and could clearly resolve the inner circumstellar environment in the  $H$ - and  $K$ -band. Besides this spectral coverage, our observations also provide a good sampling of the visibility function ( $0.8 \lesssim V \lesssim 0.1$ ) towards a wide range of position angles ( $\text{PA} = 16\text{--}113^{\circ}$ ).
- Even when considering only a single position angle, the measured visibility profile cannot be represented with the commonly applied one-component models, but indicates a more complex object geometry, likely including a disk and an envelope component.
- The measured closure phase signals (up  $\Phi \sim 40^{\circ}$ ) clearly indicate a strongly asymmetric brightness distribution.
- We find that the detected asymmetries are likely not related to the presence of a companion star, but directly trace the vertical structure of the disk around the dust sublimation radius ( $R_{\text{subl}} \sim 0.4 \text{ AU}$ ). When seen under intermediate inclination, the increased disk scale height causes obscuration and shadowing effects, which result in the observed asymmetries. To constrain the precise rim geometry, we tested three geometric and physical models, including the generic skewed ring model and rim models with a vertical and a curved rim shape. Clearly, models with a smooth brightness distribution (i.e. the skewed ring model and the curved rim model) provide a much better representation of our data than the sharp rim structure predicted by the vertical rim model.
- Confronting our data with the detailed mathematical description of the rim structure presented by IN05, we find that we can reasonably well reproduce the measured SED, as well as the visibilities and closure phases with a disk inclination angle of  $35^{\circ}$  and an incident luminosity of  $29 L_{\odot}$ . Given the absence of indications for strong active accretion, we consider that this luminosity is mainly of photospheric origin. For the dust grain size, we find that the presence of relatively large Silicate dust grains ( $\gtrsim 1.2 \mu\text{m}$ ) is required to obtain agreement between the model and our data. The derived disk position angle of  $\sim 180\text{--}190^{\circ}$  agrees well with the orientation of the polarization disk ( $\theta = 189 \pm 5^{\circ}$ ). Perpendicular to the disk axis, two bow shocks appear in the associated

<sup>3</sup> In particular, this intermediate inclination angle seems more reliable than the very low inclination of  $14^{\circ}$  determined with the skewed ring model, reflecting the fact that in the skewed ring model the dominant free parameter is the skew parameter  $s$ , while the inclination  $i$  has only a minor effect on the model appearance, and therefore, this parameter is only poorly constrained.

reflection nebula NGC 6729, suggesting that the detected disk is driving an outflow, which has shaped the bow shock-like structures.

Presenting one of the most comprehensive high-angular resolution studies on the inner structure of YSO disks, our findings provide strong evidence for the existence of a curved, puffed-up inner dust rim in Herbig Ae stars. However, additional work is needed to further constrain the detailed rim geometry and to distinguish the rim morphology from local brightness inhomogeneities, which might, for instance, be caused by hot accretion spots, spiral disk density patterns, clumpiness, or other transient phenomena. Given the complexity one likely faces on the probed sub-AU scales, this task will urgently require the model-independent aperture synthesis imaging capabilities which are just becoming available for various infrared interferometric facilities.

*Acknowledgements.* We thank the ESO Paranal team for their efforts and excellent support during our visitor mode observations and L. Testi for constructive comments, which helped to improve this paper.

## References

- Acke, B., & van den Ancker, M. E. 2004, *A&A*, 426, 151
- Acke, B., Verhoelst, T., van den Ancker, M. E., et al. 2008, *A&A*, 485, 209
- Adams, F. C., Lada, C. J., & Shu, F. H. 1987, *ApJ*, 312, 788
- Akeson, R. L., Walker, C. H., Wood, K., et al. 2005, *ApJ*, 622, 440
- Anderson, I. M., Harju, J., Knee, L. B. G., & Haikala, L. K. 1997, *A&A*, 321, 575
- Bailey, J. 1998, *MNRAS*, 301, 161
- Bellingham, J. G., & Rossano, G. S. 1980, *AJ*, 85, 555
- Bibo, E. A., The, P. S., & Dawanas, D. N. 1992, *A&A*, 260, 293
- Chen, H., Grenfell, T. G., Myers, P. C., & Hughes, J. D. 1997, *ApJ*, 478, 295
- Chiang, E. I., & Goldreich, P. 1997, *ApJ*, 490, 368
- Choi, M., Hamaguchi, K., Lee, J.-E., & Tatematsu, K. 2008, *ApJ*, 687, 406
- Clark, S., McCall, A., Chrysostomou, A., et al. 2000, *MNRAS*, 319, 337
- Dullemond, C. P., & Dominik, C. 2004, *A&A*, 417, 159
- Dullemond, C. P., Dominik, C., & Natta, A. 2001, *ApJ*, 560, 957
- Eisner, J. A., Chiang, E. I., Lane, B. F., & Akeson, R. L. 2007, *ApJ*, 657, 347
- Forbrich, J., Preibisch, T., & Menten, K. M. 2006, *A&A*, 446, 155
- García Lopez, R., Natta, A., Testi, L., & Habart, E. 2006, *A&A*, 459, 837
- Graham, J. A. 1992, *PASP*, 104, 479
- Graham, J. A. 1993, *PASP*, 105, 561
- Graham, J. A., & Phillips, A. C. 1987, *PASP*, 99, 91
- Groppi, C. E., Hunter, T. R., Blundell, R., & Sandell, G. 2007, *ApJ*, 670, 489
- Hamaguchi, K., Yamauchi, S., & Koyama, K. 2005, *ApJ*, 618, 360
- Hamidouche, M., Wang, S., & Looney, L. W. 2008, *AJ*, 135, 1474
- Hartigan, P., & Graham, J. A. 1987, *AJ*, 93, 913
- Herbig, G. H., & Bell, K. R. 1988, Catalog of emission line stars of the orion population, Lick Observatory Bulletin (Santa Cruz: Lick Observatory), 3
- Hillenbrand, L. A., Strom, S. E., Vrba, F. J., & Keene, J. 1992, *ApJ*, 397, 613
- Isella, A., & Natta, A. 2005, *A&A*, 438, 899
- Isella, A., Tatulli, E., Natta, A., & Testi, L. 2008, *A&A*, 483, L13
- Isella, A., Testi, L., & Natta, A. 2006, *A&A*, 451, 951
- Jennison, R. C. 1958, *MNRAS*, 118, 276
- Kama, M., Min, M., & Dominik, C. 2009, *A&A*, in print
- Kenyon, S. J., & Hartmann, L. 1987, *ApJ*, 323, 714
- Kraus, S., Preibisch, T., & Ohnaka, K. 2008, *ApJ*, 676, 490
- Kraus, S., Weigelt, G., Balega, Y. Y., et al. 2009, *A&A*, 497, 195
- Kurucz, R. L. 1970, SAO Special Report, 309
- Lachaume, R. 2003, *A&A*, 400, 795
- Levraut, R. M. 1988, *ApJ*, 330, 897
- Lohmann, A. W., Weigelt, G., & Wirtitzer, B. 1983, *Appl. Opt.*, 22, 4028
- Malfait, K., Bogaert, E., & Waelkens, C. 1998, *A&A*, 331, 211
- Mannings, V. 1994, *MNRAS*, 271, 587
- Marraco, H. G., & Rydgren, A. E. 1981, *AJ*, 86, 62
- Meeus, G., Waters, L. B. F. M., Bouwman, J., et al. 2001, *A&A*, 365, 476
- Millan-Gabet, R., Schloerb, F. P., & Traub, W. A. 2001, *ApJ*, 546, 358
- Millan-Gabet, R., Monnier, J. D., Berger, J.-P., et al. 2006, *ApJ*, 645, L77
- Millour, F., Petrov, R. G., Vannier, M., & Kraus, S. 2008, in *SPIE Conf. Ser.*, 7013
- Miroshnichenko, A., Ivezić, Ž., Vinković, D., & Elitzur, M. 1999, *ApJ*, 520, L115
- Monnier, J. D., & Millan-Gabet, R. 2002, *ApJ*, 579, 694
- Monnier, J. D., Millan-Gabet, R., Billmeier, R., et al. 2005, *ApJ*, 624, 832
- Monnier, J. D., Berger, J.-P., Millan-Gabet, R., et al. 2006, *ApJ*, 647, 444
- Muzerolle, J., D'Alessio, P., Calvet, N., & Hartmann, L. 2004, *ApJ*, 617, 406
- Natta, A., Palla, F., Butner, H. M., Evans, II, N. J., & Harvey, P. M. 1993, *ApJ*, 406, 674
- Natta, A., Prusti, T., Neri, R., et al. 2001, *A&A*, 371, 186
- Petrov, R. G., Malbet, F., Weigelt, G., et al. 2007, *A&A*, 464, 1
- Pinte, C., Ménard, F., Berger, J. P., Benisty, M., & Malbet, F. 2008, *ApJ*, 673, L63
- Pollack, J. B., Hollenbach, D., Beckwith, S., et al. 1994, *ApJ*, 421, 615
- Takami, M., Bailey, J., & Chrysostomou, A. 2003, *A&A*, 397, 675
- Tannirkulam, A., Harries, T. J., & Monnier, J. D. 2007, *ApJ*, 661, 374
- Tannirkulam, A., Monnier, J. D., Harries, T. J., et al. 2008, *ApJ*, 689, 513
- Tatulli, E., Millour, F., Chelli, A., et al. 2007, *A&A*, 464, 29
- Taylor, K. N. R., & Storey, J. W. V. 1984, *MNRAS*, 209, 5P
- Tuthill, P. G., Monnier, J. D., & Danchi, W. C. 2001, *Nature*, 409, 1012
- Vinković, D., & Jurkić, T. 2007, *ApJ*, 658, 462
- Vinković, D., Ivezić, Ž., Miroshnichenko, A. S., & Elitzur, M. 2003, *MNRAS*, 346, 1151
- Walker, C. K., Lada, C. J., & Hartigan, P. 1984, in *BAAS*, 16, 998
- Wang, H., Mundt, R., Henning, T., & Apai, D. 2004, *ApJ*, 617, 1191
- Ward-Thompson, D., Warren-Smith, R. F., Scarrott, S. M., & Wolstencroft, R. D. 1985, *MNRAS*, 215, 537
- Weigelt, G. P. 1977, *Opt. Commun.*, 21, 55
- Weigelt, G., & Wirtitzer, B. 1983, *Opt. Lett.*, 8, 389